Geochemistry, Geophysics, Geosystems®

Correspondence to:

A. Bessat and S. M. Schmalholz,
annelore.bessat@unil.ch;
stefan.schmalholz@unil.ch

Melt Migration and Chemical Differentiation by Reactive Porosity Waves

Annelore Bessat[1] , Sébastien Pilet[1] , Yuri Y. Podladchikov[1,2] , and Stefan M. Schmalholz[1]

[1]Institute of Earth Sciences, University of Lausanne, Lausanne, Switzerland, [2]Faculty of Mechanics and Mathematics, Moscow State University, Moscow, Russia

Abstract Melt transport across the ductile mantle is essential for oceanic crust formation or intraplate volcanism. However, mechanisms of melt migration and associated chemical interaction between melt and solid mantle remain unclear. Here, we present a thermo-hydro-mechanical-chemical (THMC) model for melt migration coupled to chemical differentiation. We consider melt migration by porosity waves and a chemical system of forsterite-fayalite-silica. We solve the one-dimensional (1D) THMC model numerically using the finite difference method. Variables, such as solid and melt densities or MgO and SiO_2 mass concentrations, are functions of pressure (P), temperature (T), and total silica mass fraction ($C_T^{SiO_2}$). These variables are pre-computed with Gibbs energy minimization and their variations with evolving P, T, and $C_T^{SiO_2}$ are implemented in the THMC model. We consider P and T conditions relevant around the lithosphere-asthenosphere boundary. Systematic 1D simulations quantify the impact of initial distributions of porosity and $C_T^{SiO_2}$ on the melt velocity. Larger perturbations of $C_T^{SiO_2}$ cause larger melt velocities. An adiabatic or conductive geotherm cause fundamentally different vertical variations of densities and concentrations, and an adiabatic geotherm generates higher melt velocities. We quantify differences between melt transport (considering incompatible tracers), major element transport and porosity evolution. Melt transport is significant in the models. We also quantify the relative importance of four porosity variation mechanisms: (a) mechanical compaction and decompaction, (b) density variation, (c) compositional variation, and (d) solid-melt mass exchange. In the models, (de)compaction dominates the porosity variation. We further discuss preliminary results of 2D THMC simulations showing blob-like and channel-like porosity waves.

Plain Language Summary Melt transport across the ductile mantle is essential for oceanic crust formation or intraplate volcanism. However, melt transport processes are still incompletely understood and poorly quantified. Xenoliths (inclusions in igneous rock entrained during magma ascent) sampled by kimberlites (an igneous rock that erupted from the mantle) or intraplate basalts provide evidence that there is a reaction (metasomatism) between the rising melt and the solid mantle. However, the impact of chemical processes on melt migration remains unclear. Here, we present a new mathematical two-phase (fluid-solid) model, based on fundamental laws of physics and thermodynamics, which couples melt migration with chemical processes. We study melt migration around the lithosphere-asthenosphere boundary and consider the solid (not molten) rocks as highly viscous fluids due to the high temperatures in these regions (at 80–100 km depth). We present one-dimensional results of computer simulations and show that the variation of chemical components, such as silicon dioxide, changes the densities of the solid and melt, and can, hence, have a considerable impact on melt migration. We also present two-dimensional simulations, which show the channelization of the rising melt.

1. Introduction

The extraction of melt from its sources and melt transport across the mantle to the surface is a key process in Earth sciences (e.g., Keller & Suckale, 2019; McKenzie, 1984; Schmeling et al., 2019; Spiegelman et al., 2001). The different geodynamic settings with magmatism observed around the world, such as mid-ocean ridges (MORs), volcanic arcs and intraplate volcanism, indicate that asthenospheric melts are extracted under significantly distinct pressure, temperature and rheological conditions (Figure 1a). The main difference between melt extraction at intraplate settings and at MORs is the presence of the lithospheric mantle for the intraplate settings. The geochemical signature of MOR basalt (MORB) presumably depends on magma source composition, melt-extraction and differentiation processes intervening between the magma source and the crust (e.g., Langmuir et al., 1992). MORBs are produced and migrate in the asthenosphere and temperature (T) and pressure (P) variations are,
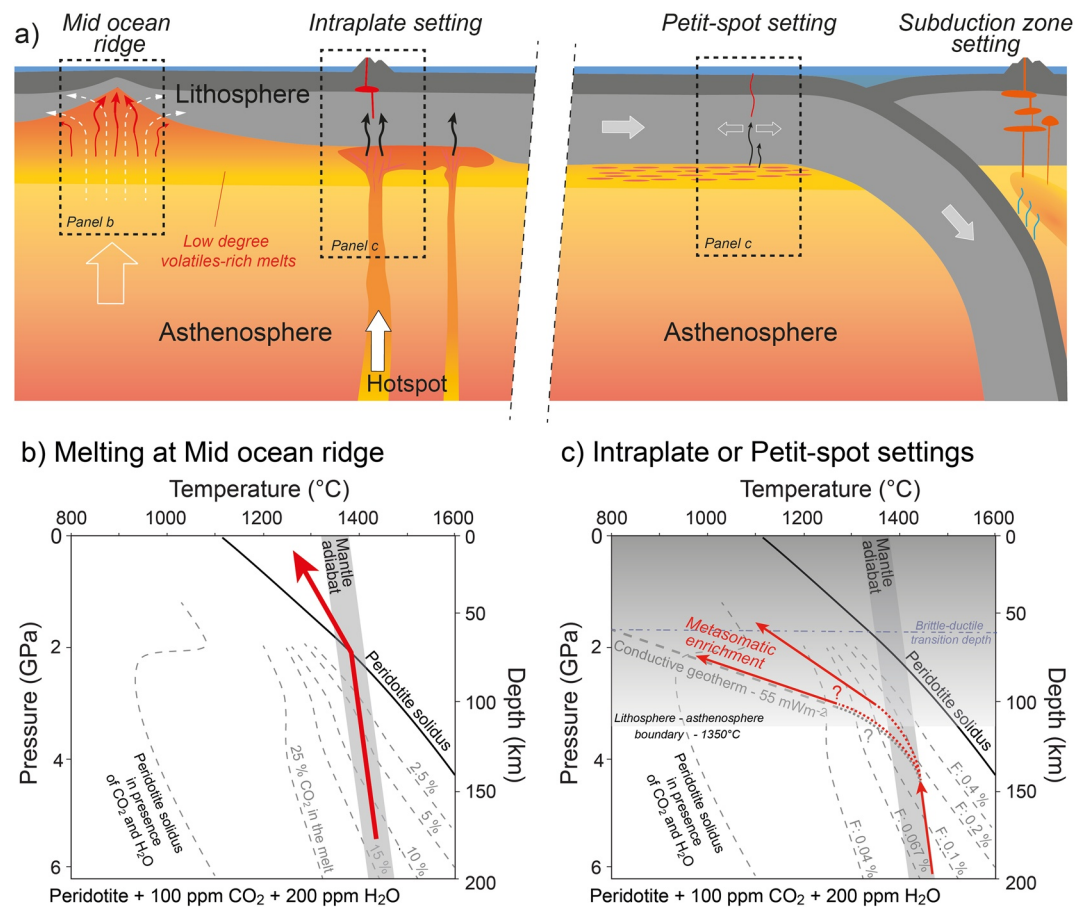
Figure 1. (a) Sketch illustrating different geodynamic settings for melt migration and volcanism. P–T diagrams illustrating the melting below (b) mid ocean ridges and (c) in intraplate setting. Dashed lines show carbonated melt isopleths as function of CO_2 content in the melt (panel b) or as function of the degree of partial melting (F, panel c) calculated by Dasgupta (2018) for a homogeneous mantle containing 200 ppm of H_2O and 100 ppm of CO_2. Solidus for a dry mantle (Hirschmann et al., 2003) or for hydrous carbonated peridotite (Wallace & Green, 1988) are shown as references. The red arrow in panel b shows the P–T melt path for mantle upwelling below a mid ocean ridge, while the red arrows (panel c) show the potential path for melt rising into the lithosphere. This path will depend on the velocity of the rising melts and its thermal equilibration with the surrounding mantle. If melts follow the conductive geotherm, metasomatic enrichment of the lithosphere associated with the cooling and crystallization of the rising magma is expected. Dark gray line reports lithospheric geotherm corresponding to a heat flux of 55 mWm^{-2} typical for old oceanic plate. Blue dashed line indicates the estimation of the brittle-ductile transition depth in oceanic lithosphere from Bessat et al. (2020).

hence, controlled by the mantle adiabat (Figure 1). In contrast, asthenospheric melts produced in intraplate settings need to cross the continental or oceanic lithosphere before their extraction to the surface (Figure 1). For example, petit-spot volcanoes, interpreted as low-degree melt extracted from the low-velocity zone in response to plate flexure (Hirano et al., 2006), could correspond to an endmember of the diversity of intraplate volcanoes observed in oceanic and continental settings. Figure 1b and 1c show the distribution of melts as function of pressure and temperature for peridotite containing 200 ppm of H_2O and 100 ppm of CO_2, contents similar to estimated values for the convecting, depleted upper mantle (50–150 ppm H_2O; 25–100 ppm CO_2; Hirschmann, 2010). Progressive extraction of melts at MORs happens under increasing melt fraction conditions as the mantle adiabat intersects the dry peridotite solidus at 60–70 km depth. The fact that melts move always in the direction of the P–T conditions promoting mantle melting helps the melts to rise and to be extracted to the surface (Figure 1b). The conditions are different for melt extraction in intraplate settings due to the presence of the lithosphere (Figure 1c).

The lithosphere is characterized by a strong temperature gradient and the associated vertical rheological variations from viscous to elasto-plastic domains (e.g., Burov, 2011). Petrological constraints (e.g., Dasgupta, 2018; Hirschmann, 2010) indicate the presence of small degree melts at the top of the asthenosphere in response to the
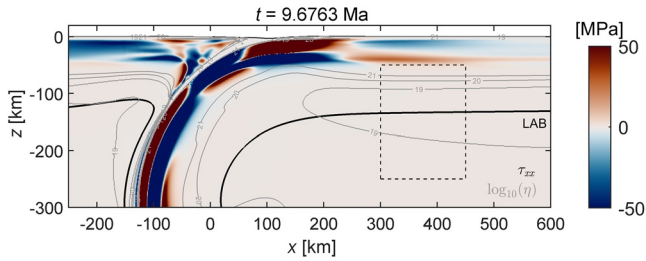
Figure 2. Representative results of a thermo-mechanical numerical subduction simulation from Bessat et al. (2020). Colorplot shows horizontal deviatoric stress (positive for extension in red) and gray contour lines indicate the logarithm to the base 10 of the viscosity (in Pa·s). The dashed rectangle indicates a region around the LAB (defined by 1,440°C isotherm) in which deviatoric stresses are negligible and the viscosity is in the order of 10^{19} Pa·s. This region corresponds to a geodynamic setting in which petit-spot volcanism can be initiated (see Figure 1a).

effect of volatiles that depress the melting solidus of peridotite with respect to dry conditions. The amount of melt increases slowly while the melt CO_2 content decreases to the top of the asthenosphere. In contrast, the amount of melt potentially present in the lithosphere decreases quickly according to the slope of the lithospheric geotherm (Figure 1c). Thermo-mechanical numerical simulations of oceanic subduction, recently performed by Bessat et al. (2020), allow to assess the rheological conditions at the lithosphere-asthenosphere boundary (LAB) in the horizontal regions of the subducting lithosphere, relevant for petit-spot volcanism (Figure 1a; dashed black rectangle in Figure 2). The numerical results indicate that the main rheological changes are not observed around the LAB (indicated by the 1,440°C isotherm), but at mid lithosphere depth, at ~60 km (Figure 2). This depth is characterized by a strong increase in the absolute magnitude of deviatoric stresses (Figure 2) indicating a rheological change from ductile (lower region) to elastic-plastic (upper region) dominated deformation mechanisms (Bessat et al., 2020). The numerical results also show that the solid viscosity around the LAB is in the order of 10^{19} Pa·s. These results further suggest that melt rising from the top of the asthenosphere needs to percolate across a large ductile region before potentially being extracted to the surface by hydrous fractures from the middle of the lithosphere to the surface. As schemed in Figure 1c, the evolution of rising magmas will depend on its P-T path (Figure 1c). If melts follow the conductive geotherm, such melts will cool and crystallize, producing metasomatic enrichment of the base of the lithosphere as documented in mantle xenoliths from the Pacific plate sampled by petit-spot magmas (Pilet et al., 2016). This metasomatic enrichment is critical to understand the chemical signature of alkaline lavas observed in intraplate setting melts as documented by various petrological studies (e.g., Pilet et al., 2008; Wass & Roge, 1980), but the mechanical aspects of this percolation remain poorly constrained.

The ductile region around the LAB includes the thermal boundary layer (Figure 1b) corresponding to the zone where the geotherm changes from adiabatic (convective) to conductive. Melt migration in the ductile domain is presumably controlled by porous flow in a viscous solid (e.g., McKenzie, 1984), while hydrous fractures propagating into the brittle domain allow melt transport to the surface (e.g., Keller et al., 2013; Shaw, 1980). Only few studies have focused on the mechanism of extraction and transport of melt across a thick and cold lithosphere, considering a visco-elasto-plastic deformation behavior (e.g., Keller et al., 2013). Hence, many aspects of the thermo-hydro-mechanical (THM) process of melt migration across the lithosphere are poorly constrained.

In addition to THM processes, melt migration can be affected by chemical (C) reactions, leading to a reactive melt flow (e.g., Jackson et al., 2018). For example, crystallization can cause changes in the porosity and, hence, change the permeability during reactive melt flow (e.g., Aharonov et al., 1997). Also, low-viscosity magma, like carbonatite or volatile-rich low degree silicate melts, can rise in the upper mantle. However, such low-degree melts cannot transport significant heat (McKenzie, 1985) and if such melts rise in the lithospheric mantle with a considerable geothermal gradient (Figure 1b) then these melts likely interact with the surrounding solid mantle, cool, and crystallize. This melt-solid interaction is frequently referred to as metasomatism and was documented by various xenoliths sampled by kimberlites or intraplate basalts worldwide (e.g., Best, 1974; Francis, 1976; Irving, 1980; Lloyd & Bailey, 1975). Metasomatic processes are important to understand the chemical evolution of the continental lithosphere (e.g., Griffin et al., 2009) and the petrogenesis of alkaline lavas (e.g., Lloyd & Bailey, 1975; Pilet et al., 2008; Wass & Roge, 1980). However, the origin of the metasomatic agent(s), the process by which low degree melts percolate across the lithosphere, and whether metasomatic processes represent a global mechanism at the LAB are still a matter of debate. Therefore, we aim here to investigate coupled reactive transport during melt migration around the LAB.

From a geometrical point of view, there are two general styles of flow during melt migration in a viscous domain: (a) a spatially distributed flow, characterized by a pervasive percolation of melt between the crystals of the solid rock (e.g., olivine or pyroxene crystals in a peridotite) and (b) a spatially focused flow where melt migration is localized in channels, which is documented in the mantle by the presence of metasomatic veins (Harte et al., 1993; Wilshire, 1987). According to the lithosphere thermal gradient, rising melt cools progressively and crystallizes mineral phases which are segregated within the lithospheric mantle, producing metasomatic cumulates sampled

by intraplate lavas or observed in mantle outcrops (e.g., Harte et al., 1993; Nielson & Noller, 1987; Nielson & Wilshire, 1993; Wilshire, 1987). Both distributed and focused flows involve a change in the composition of the melt due to its interaction with the solid. For distributed flow, the change of composition is achieved by the infiltrating melt that reacts with the peridotite through an exchange of elements (so-called cryptic metasomatism; Wilshire, 1987). For focused flow, the change in melt composition predominantly occurs by differentiation as phases crystallize (so called percolative fractional crystallization; Harte et al., 1993). Most models for the metasomatic enrichment were developed based on observations made in the brittle part of the lithosphere. How metasomatic agents move into the ductile part of the mantle, how such melt interacts with the solid and how channels are generated are still open to debate.

From a physical point of view, the rise of large coherent magma bodies in a viscous solid can be described by diapiric flow (e.g., Cruden, 1988; Dohmen & Schmeling, 2021; Miller & Paterson, 1999; Weinberg & Podladchikov, 1994). However, the physical process of melt extraction and migration in partially molten viscous rock is commonly described by two-phase flow models whereby the melt, representing the fluid phase, flows through the pore space of the viscous rock, representing the solid phase (e.g., McKenzie, 1984; Schmeling et al., 2019). There are several potential extraction processes for melt migration in a porous, ductile rock: (a) porous flow, described by Darcy's law, controlled by the rate of melt expulsion whereby the characteristics of solid deformation are of minor importance (e.g., Ahern & Turcotte, 1979; Walker et al., 1978), (b) melt transport by porosity waves for which volumetric deformation of the viscous solid is essential (e.g., Connolly & Podladchikov, 1998, 2007; Dohmen et al., 2019; Jordan et al., 2018; Keller et al., 2013; McKenzie, 1984; Omlin et al., 2017; Scott & Stevenson, 1984; Spiegelman, 1993; Yarushina & Podladchikov, 2015), (c) melt migration by reaction infiltration instabilities controlled by depth-dependent solubilities (e.g., Aharonov et al., 1995, 1997; Jones & Katz, 2018; Kelemen et al., 1997; Spiegelman et al., 2001; Weatherley & Katz, 2012) or porosities (e.g., Jordan & Hesse, 2015), (d) extraction by shear localization and melt segregation generating melt bands (e.g., Holtzman & Kohlstedt, 2007; Katz et al., 2006; Stevenson, 1989), and (e) melt ascent due to a combination of compaction and decompaction of the contact zones between accumulated magma and solid rock that dislodges solid material from the roof that sinks through and partly dissolves in the magma (Schmeling et al., 2019).

We focus here on melt migration by porosity waves. Porosity waves are an ubiquitous feature arising from the governing equations of compressible two-phase flow (e.g., McKenzie, 1984; Scott & Stevenson, 1984). Such waves have been observed in analogue experiments (e.g., Scott et al., 1986) and have been proposed as mechanism forming observed seismic chimneys above hydrocarbon reservoirs (e.g., Yarushina et al., 2021). Connolly and Podladchikov (1998) show that employing a visco-elastic volumetric deformation of the solid enables porosity waves to travel through rock in the limit of zero initial connected porosity. Low-porosity (i.e., few percent) scenarios are most relevant for melt migration across the viscous mantle. The application of decompaction weakening (e.g., Connolly & Podladchikov, 1998, 2007) and the consideration of viscous shear deformation of the solid (Räss et al., 2019) enables a significant channelization of porosity waves for two- and three-dimensional (2D and 3D) flow. Furthermore, Omlin et al. (2017) show that the coupling of the kinetics of chemical reactions with fluid flow may enable porosity waves also to potentially arise in low-temperature regimes, so that the porosity waves are not necessarily limited to the high-temperature viscous regions (Chakraborty, 2017). Moreover, Jordan et al. (2018) show that mass, and hence melt, can be transported in 2D and 3D porosity waves; a fact that has been doubted based on 1D porosity wave studies. Therefore, porosity waves are a potential mechanism to transport significant melt in a channelized style across the LAB and the viscous lithospheric mantle.

Here, we present a new numerical thermo-hydro-mechanical-chemical (THMC) model to investigate reactive melt migration by porosity waves in a viscous solid coupled to heat transfer and to chemical differentiation of major elements in the melt and solid. Chemical differentiation of major elements is important for melt migration because it changes, for example, the density of the melt and solid or it can change the porosity, which could cause a significant reduction of permeability (clogging). Such density variations do not occur for trace element transport by porosity waves (e.g., Jordan et al., 2018) applied to study, for example, the chromatographic separation occurring during percolation (Hofmann, 1972; Korzhinskii, 1965), because trace elements do not alter the density or porosity of melt and solid. The importance of chemical differentiation for the rise of magma in the crust has been highlighted recently by Jackson et al. (2018). We couple our THMC model with thermodynamic results calculated by Gibbs energy minimization. We perform this minimization with a self-developed MATLAB code using a linear programming algorithm. The P and T conditions are chosen to reflect conditions at the LAB. We
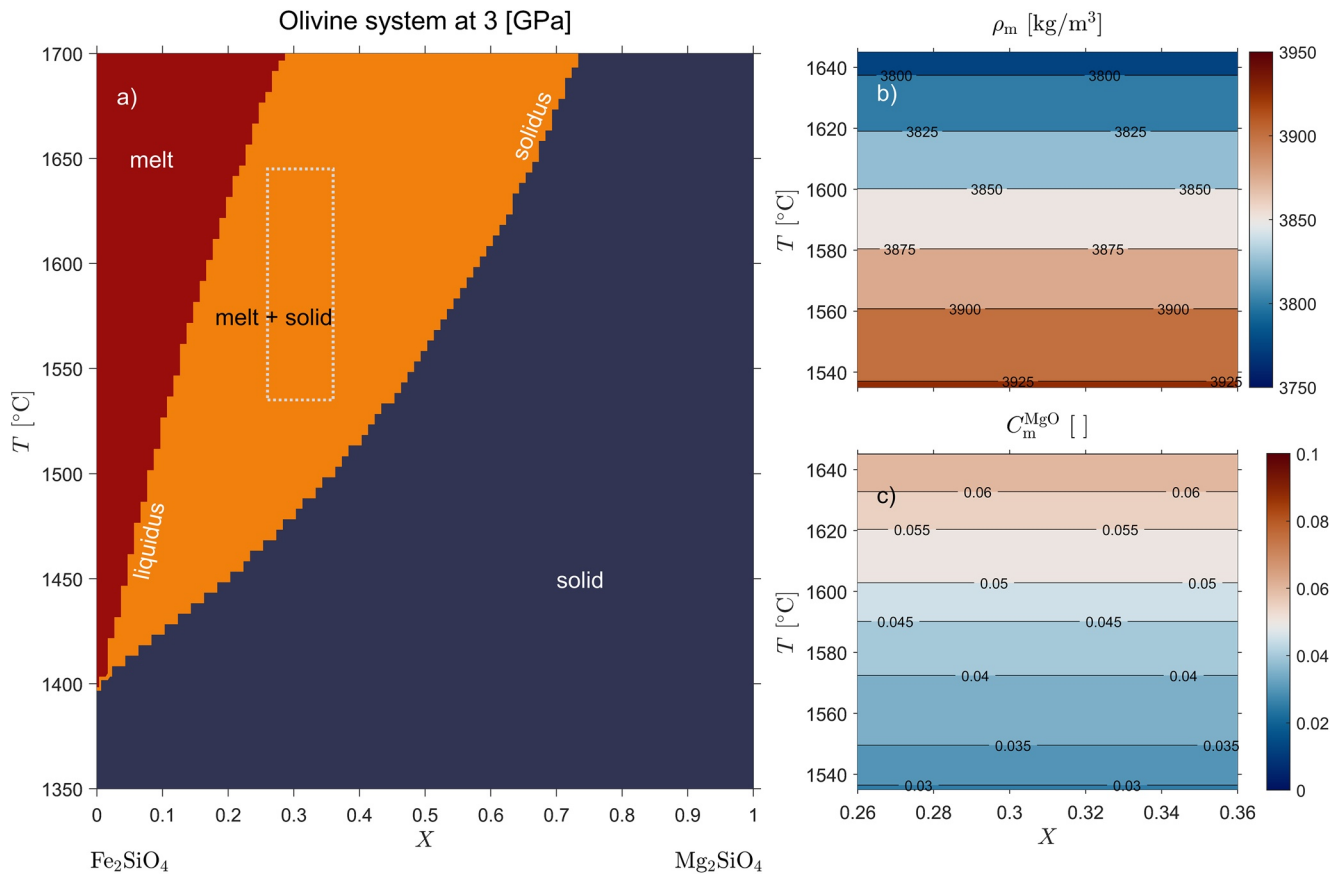
Figure 3. Panel (a) shows the binary system of olivine for a pressure of 3 GPa in the space mole fraction of forsterite versus temperature (X vs. T). X is the mole fraction of forsterite. Blue area shows where solid is stable, red area shows where melt is stable and orange area shows where both solid and melt are stable (i.e., region of partial melting). Dashed square indicates the region used to calculate thermodynamic variables employed in the thermo-hydro-mechanical-chemical model. Panels (b and c) show respectively, the melt density and the melt mass fraction of magnesium (in the dashed region), which are independent on X in the region of interest.

consider a simple ternary system composition of MgO, FeO, and SiO$_2$ based on the olivine phase diagram system, forsterite (Mg$_2$SiO$_4$) and fayalite (Fe$_2$SiO$_4$). We consider conditions for which the system is always between solidus and liquidus so that both melt and solid phases are present simultaneously (Figure 3). We extend this binary system by adding more SiO$_2$ using experimental data of peridotite in equilibrium with melt at 3 GPa (Davis et al., 2011). The model variables determined by thermodynamic calculations (e.g., solid and melt densities, mass fractions of MgO and SiO$_2$ of the melt and the solid) are fully variable and are a function of P, T, and chemical SiO$_2$ composition of the system ($C_\mathrm{T}^{\mathrm{SiO_2}}$). These variables and their dependence of P, T, and SiO$_2$ are precomputed and used in the THMC reactive transport model, so that they can evolve freely with evolving P, T, and SiO$_2$. The model, hence, allows quantifying the impact of variations in the chemical composition on melt migration. We use here the term THMC model to emphasize (a) the general applicability of the model approach (e.g., application to dehydration reactions in deforming rock by Schmalholz et al. (2020)), (b) the full mobility and dependency of densities and mass fractions on P, T, and SiO$_2$, (c) the consideration of solid deformation, and (d) the coupling of a two-phase transport model with thermodynamic phase calculations.

The aims of our study are: (a) to present a new numerical THMC model for coupled melt migration and chemical differentiation by reactive porosity waves, (b) to explain specific features of coupling chemical differentiation with porosity waves, such as mechanisms of porosity variation and mass transport, and (c) to discuss potential applications of our model to melt migration around the LAB for different geotherms. We present the model derivation and some systematic results for 1D and show preliminary results of 2D simulations, showing blob- and channel-like reactive porosity waves.

2. Mathematical Model

We develop a 1D mathematical model for THMC reactive transport by porosity waves. The model is based on the concepts of continuum mechanics, two-phase flow and equilibrium thermodynamics and follows the same approach in deriving a closed system of equations as described in Yarushina and Podladchikov (2015), Malvoisin et al. (2015), or Schmalholz et al. (2020). The complete THMC model consists of two parts: (a) a THMC model for two-phase reactive transport of melt by porosity waves, which is described by a system of partial differential equations. (b) A thermodynamic model, which is based on Gibbs energy minimization. This thermodynamic model provides the required solid and melt densities as well as the solid and melt mass fractions of MgO and SiO$_2$. These densities and mass fractions all vary with varying P, T, and $C_T^{SiO_2}$. Furthermore, the thermodynamic model provides the specific heat for melt and solid required for the temperature calculation.

2.1. Thermodynamic Model

We apply a thermodynamic model to determine the stable phases for a range of P, T, and composition (X). We start with a simple binary system of olivine (Figure 3a) between forsterite, the olivine magnesium-rich end-member (Mg$_2$SiO$_4$), and fayalite, the olivine iron-rich end-member (Fe$_2$SiO$_4$).

We minimize the Gibbs free energy, G, to determine the equilibrium of the binary system. The Gibbs free energies used for the minimization are calculated with four endmembers, taken from the thermodynamic database of Holland and Powell (1998), and ideal and mechanical mixing models for solid and melt. To calculate this minimization, we use the linear programming "linprog" algorithm from MATLAB. We consider a pressure range of 0.1–4.9 GPa and a temperature range of 1,200°C–1,700°C. The X composition specifies the mole fraction of forsterite and varies from 0 to 1, with 0 corresponding to 100% of fayalite and 0% of forsterite and 1 corresponding to 0% fayalite and 100% of forsterite. There are four phase endmembers in this two-phase solid-melt system; for the solid part there are forsterite (fo) and fayalite (fa), and for the melt (liquid) part there are forsterite (foL) and fayalite (faL) (see Holland & Powell, 1998 for nomenclature). Figure 3a shows the result of the minimization and emphasizes where the phases are stable for a pressure of 3 GPa. After the minimization of G, in each point of the P–T–X domain, we extract several quantities for the melt (with subscript m) and the solid (with subscript s; all listed in Table 1): Gibbs energy, G_m and G_s in (J mol^{-1}), volume, V_m and V_s in (m^3 mol^{-1}), entropy, S_m and S_s in (J mol^{-1} K^{-1}) and specific heat capacity, C_{p_m} and C_{p_s} in (J mol^{-1} K^{-1}). We calculate the quantities from the Gibbs energies, volume $V_{m,s} = \frac{\partial G_{m,s}}{\partial P}|_T$ and entropy $S_{m,s} = -\frac{\partial G_{m,s}}{\partial T}|_P$. The specific heat capacity $C_{p_{m,s}} = T\frac{\partial S_{m,s}}{\partial T}|_P$. To have all parameters in mass units of kilogram, and not in mole, we divide all quantities by their respective melt or solid molar mass, m_m and m_s in (kg mol^{-1}), which are computed from molar masses of forsterite, fayalite and silica endmembers, and compositions of solid and melt. With the specific volume, we can then calculate melt and solid density, $\rho_{m,s} = 1/V_{m,s}$ in (kg m^{-3}). In addition, several molar fractions (in mole units) can be obtained from Gibbs minimization, like melt concentrations of forsterite and fayalite, $C_{m,[mol]}^{foL}$ and $C_{m,[mol]}^{foL}$, and solid concentrations of forsterite and fayalite, $C_{s,[mol]}^{fo}$ and $C_{s,[mol]}^{fa}$. We transform them into mass fractions to use them in the mass conservation equations of the THMC model. The details of this transformation are presented in Appendix D, Equations D1–D3.

In the THMC model, we focus on the thermodynamic region where melt and solid coexist, inside the phase loop (orange area in Figure 3a). In the considered P–T–X domain, this region has a pressure range of 2.4–3.5 GPa, a temperature range of 1,535°C (1,808.15 K) to 1,645°C (1,918.15 K) and a composition range of 0.26–0.36. Figures 3b and 3c show that the variation in melt density (ρ_m) and in melt mass fraction of magnesium (C_m^{MgO}), respectively, are independent of composition (X) inside the phase loop (constant values of ρ_m and C_m^{MgO} as function of X). Accordingly, all other thermodynamic parameters used in the THMC model are also independent of composition, such as solid density (ρ_s), solid mass fraction of magnesium (C_s^{MgO}) and melt and solid mass fractions of silica ($C_m^{SiO_2}$, $C_s^{SiO_2}$). Therefore, for our binary system, we can reduce the three-dimensional P–T–X parameter space to a two-dimensional P–T parameter space for all thermodynamically predicted densities, mass fractions and heat capacities (Table 2). The independency of densities and mass fractions on composition X is a result of the Gibbs phase rule (e.g., Müller, 2007) because there is no degree of freedom for a system with two components (fo and fa) and two phases (solid and melt) for a given temperature and pressure.

In the THMC transport model, described in the next section, we will use the solid and melt densities and the solid and melt mass fractions for magnesium and silica, which will all be a function of P, T, and $C_T^{SiO_2}$. We describe the densities and mass fractions as a linear function of P, T, $C_T^{SiO_2}$. For example, the melt density is described by the linear function,

Table 1
Parameters Used in the Thermodynamic and THMC Model

Symbol	Meaning	Units
ρ_m, ρ_s, and ρ_T	Melt, solid, and total densities	kg·m⁻³
C_m^{MgO}, C_s^{MgO}, $C_m^{SiO_2}$, $C_s^{SiO_2}$	Mass fractions of magnesium or silica for melt and solid	( )
U_m and U_s	Melt, solid thermal energies	J·mol⁻¹
C_{p_m}, C_{p_s}	Melt, solid specific heat capacity	J·kg⁻¹·K⁻¹
λ_m, λ_s, λ_T	Melt, solid, and total thermal conductivity	W·m⁻¹·K⁻¹
G_m, G_s	Melt, solid Gibbs energies	J·mol⁻¹
V_m, V_s	Melt and solid volumes	m³·mol⁻¹
S_m, S_s	Melt and solid entropy	J·mol⁻¹·K⁻¹
m_m, m_s	Melt and solid molar mass	kg¹·mol⁻¹
k	Permeability	m²
φ	Porosity	( )
υ_m, υ_s	Melt and solid velocity	m·s⁻¹
σ_{xx}	Total stress	Pa
τ	Deviatoric stress	Pa
g	Gravitational acceleration	m·s⁻²
P_T, P_m, P_e	Total pressure, melt pressure, and effective pressure	Pa
η_s, η_v, η_m	Shear viscosity, bulk viscosity, and melt viscosity	Pa·s
t	Time	s
T	Temperature	K

Note. THMC, thermo-hydro-mechanical-chemical.

Table 2
Values for Linear Approximation of Thermodynamic Variables

Adopted values for linearization						
P_0				3.0001·10⁹		(Pa)
T_0				1,863.15		(K)
$C_{T,0}^{SiO_2}$				0.3280		( )

Value at reference point		Alpha (K⁻¹)		Beta (Pa⁻¹)		Gamma ( )	
$\rho_{m,0}$	3.8631·10³ (kg m⁻³)	$^\alpha\rho_m$	−3.3260·10⁻⁴	$^\beta\rho_m$	3.2666·10⁻¹¹	$^\gamma\rho_m$	−1.0700
$\rho_{s,0}$	3.6401·10³ (kg m⁻³)	$^\alpha\rho_s$	−6.5732·10⁻⁴	$^\beta\rho_s$	4.7575·10⁻¹¹	$^\gamma\rho_s$	−0.3791
$C_{m,0}^{MgO}$	0.0449 ( )	$\alpha_{C_m^{MgO}}$	0.0073	$\beta_{C_m^{MgO}}$	−3.3051·10⁻¹⁰	$\gamma_{C_m^{MgO}}$	17.0251
$C_{s,0}^{MgO}$	0.2232 ( )	$\alpha_{C_s^{MgO}}$	0.0047	$\beta_{C_s^{MgO}}$	−2.9722·10⁻¹⁰	$\gamma_{C_s^{MgO}}$	3.7930
$C_{m,0}^{SiO_2}$	0.3079 ( )	$\alpha_{C_m^{SiO_2}}$	2.3932·10⁻⁴	$\beta_{C_m^{SiO_2}}$	−1.0870·10⁻¹¹	$\gamma_{C_m^{SiO_2}}$	4.5448
$C_{s,0}^{SiO_2}$	0.3481 ( )	$\alpha_{C_s^{SiO_2}}$	6.8708·10⁻⁴	$\beta_{C_s^{SiO_2}}$	−4.3008·10⁻¹¹	$\gamma_{C_s^{SiO_2}}$	1.7257
$C_{p_m,0}$	1.2481·10³ (J kg⁻¹ K⁻¹)						
$C_{p_s,0}$	1.1940·10³ (J kg⁻¹ K⁻¹)						

Note. Values are calculated from Gibbs free energy minimization and the experiment of Davis et al. (2011), see Section 2.1 for details.

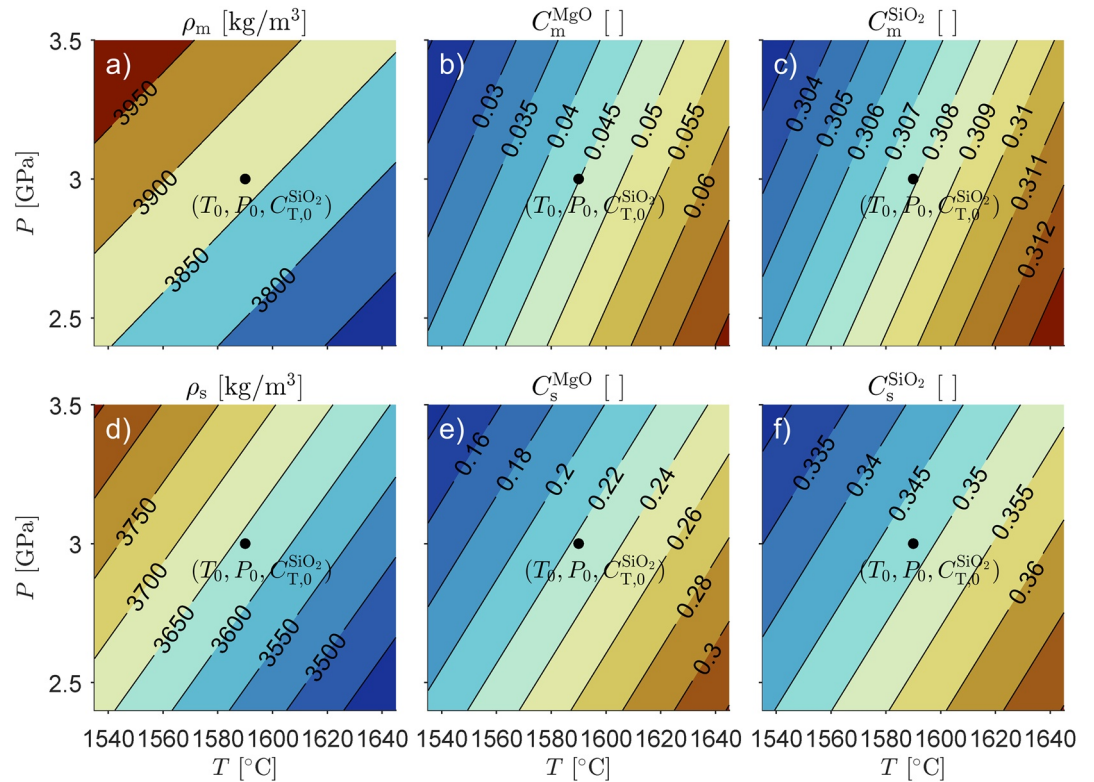**Figure 4.** Linear approximation of densities and mass fractions using thermal expansion coefficient, α, and compressibility, β (see Equations 1, 2 and 3). All parameters vary with temperature and pressure: panel (a) melt density, panel (d) solid density, panel (b) mass fraction of magnesium in melt, panel (e) mass fraction of magnesium in solid, panel (c) mass fraction of silica in melt, and panel (f) mass fraction of silica in solid. Black point in the center of each panel is the reference point at T_0, P_0, and $C_{T,0}^{SiO_2}$. $C_{T,0}^{SiO_2}$ corresponds to the total mass fraction of silica in the olivine.

$$\rho_m = \rho_{m,0} \left(1 + \alpha_{\rho_m} \Delta T + \beta_{\rho_m} \Delta P + \gamma_{\rho_m} \Delta C_T^{SiO_2} \right) \tag{1}$$

The parameters α, β, and γ determine the dependency of the melt density on P, T, and $C_T^{SiO_2}$, respectively. Their subscripts ρ_m indicate that the values of α, β, and γ apply to the melt density. The $\rho_{m,0}$ is the reference melt density for a given reference P_0, T_0, and $C_{T,0}^{SiO_2}$ (Table 2). The ΔT, ΔP, and $\Delta C_T^{SiO_2}$ are the differences of P, T, and $C_T^{SiO_2}$ from the respective reference values. For the solid density and the four mass fractions, similar linearized equations are applied, but with different values of α, β, and γ (Table 2 and Section 3). We use the linearized relations instead of the results obtained directly from the Gibbs free energy minimization (Figure 4), mainly for simplicity reason. Furthermore, the parameters α, β, and γ for the different densities and mass fractions provide a quantitative and transparent insight into the relative dependencies of densities and mass fractions on P, T, and $C_T^{SiO_2}$ (see Section 3). If values of α, β, or γ are positive, then the corresponding parameter will increase with the respective increase of P, T, and $C_T^{SiO_2}$ (e.g., in Figure 4, ρ_m increases with increasing pressure, since β_{ρ_m} is positive). Consequently, if values α, β, or γ are negative, then the associated parameter will decrease with the respective increase of P, T, and $C_T^{SiO_2}$ (e.g., in Figure 4, ρ_m decreases with increasing temperature since α_{ρ_m} is negative).

In the following, we describe first how we calculate the values of α and β from the thermodynamic results for olivine (Figure 3). Next, we describe how we calculate the values of γ using a melting experiment by Davis et al. (2011).

The α and β for the six variables (two densities and four mass fractions) are calculated, for example, for the melt density by:

$$\alpha_{\rho_m} = \left(\frac{\rho_m(2, P_0) - \rho_m(1, P_0)}{\Delta T} \right) \Big/ \rho_{m,0} \tag{2}$$

$$\beta_{\rho_m} = \left(\frac{\rho_m(T_0, 2) - \rho_m(T_0, 1)}{\Delta P} \right) \bigg/ \rho_{m,0} \tag{3}$$

where ΔT and ΔP are the temperature and pressure differences of domain P–T, $\rho_m(2,P_0) - \rho_m(1,P_0)$ is density variation as function of temperature, $\rho_m(T_0,2) - \rho_m(T_0,1)$ is density variation as function of pressure and $\rho_{m,0}$ is the density at the reference point T_0 and P_0 (Table 2). $\rho_m(1,P_0)$ is calculated at a temperature of 1,535°C and $\rho_m(2,P_0)$ at 1,645°C, whereas $\rho_m(T_0,1)$ is calculated at a pressure of 2.4 GPa and $\rho_m(T_0,2)$ at 3.5 GPa. The same procedure is applied for the other five variables: the resulting values for α and β are given in Table 2 and are further discussed in the result section. Figure 4 illustrates the results of the linearization for each variable in the space P–T.

A particular result for binary olivine in the considered P and T range is that solid density is smaller than melt density (Figures 4a and 4d). This density relation is a known phenomenon in the forsterite-fayalite system for high temperature (e.g., Herzberg et al., 1982). For melt to rise, it should have a smaller density than the solid. To obtain smaller melt densities, we add another composition dimension to our P–T domain, which is the total silica mass fraction $C_T^{SiO_2}$. Adding more silica to the olivine system allows to change the melt and solid densities of the system to a more realistic value for a peridotitic system. For simplicity, we did not include pyroxenes in our thermodynamic calculation.

The value of $C_{T,0}^{SiO_2}$ is calculated at the reference point T_0 and P_0 as follows:

$$C_{T,0}^{SiO_2} = \frac{C_{m,0}^{SiO_2} + C_{s,0}^{SiO_2}}{C_{m,0}^{MgO} + C_{s,0}^{MgO} + C_{m,0}^{FeO} + C_{s,0}^{FeO} + C_{m,0}^{SiO_2} + C_{s,0}^{SiO_2}} \tag{4}$$

By increasing $C_T^{SiO_2}$, the density of melt will become smaller than the density of solid, allowing the melt to percolate toward the surface. We use the experiment by Davis et al. (2011) which provides the composition of a peridotite in equilibrium with the first magma produced by partial melting at a P of 3 GPa and a T of 1,450°C. These experimental compositions are reported as "KLB-1ox" for the solid, and "0% melt" for melt in Table 1 of Davis et al. (2011). The combination of these data and the values obtained by our thermodynamic olivine model allows calculating a γ parameter that quantifies the variation of the six variables (ρ_m, ρ_s, C_m^{MgO}, C_s^{MgO}, $C_m^{SiO_2}$, and $C_s^{SiO_2}$) as function of $C_T^{SiO_2}$ in the system. To calculate γ for mass fractions of magnesium or silica for melt and solid, we transform the MgO, FeO, and SiO$_2$ oxides weight percent of "KLB-1ox" and "0% melt" into oxides mass fractions (here shown for MgO; the same procedure is applied for FeO and SiO$_2$):

$$C_{m,exp}^{MgO} = \frac{C_{0\%\ melt,[wt\%]}^{MgO}}{C_{0\%\ melt,[wt\%]}^{MgO} + C_{0\%\ melt,[wt\%]}^{FeO} + C_{0\%\ melt,[wt\%]}^{SiO_2}} \tag{5a}$$

$$C_{s,exp}^{MgO} = \frac{C_{KLB-1ox,[wt\%]}^{MgO}}{C_{KLB-1ox,[wt\%]}^{MgO} + C_{KLB-1ox,[wt\%]}^{FeO} + C_{KLB-1ox,[wt\%]}^{SiO_2}} \tag{5b}$$

The total silica mass fraction of the experiment, $C_{T,exp}^{SiO_2}$, is calculated in the same way as shown in Equation 4. Then, we calculate the γ (here shown for C_m^{MgO} and C_s^{MgO}; the same procedure applies for $C_m^{SiO_2}$ and $C_s^{SiO_2}$ shown in Appendix D, Equation D4) by:

$$\gamma_{C_m^{MgO}} = \left(\frac{C_{m,exp}^{MgO} - C_{m,0}^{MgO}}{C_{T,exp}^{SiO_2} - C_{T,0}^{SiO_2}} \right) \bigg/ C_{m,0}^{MgO} \tag{6a}$$

$$\gamma_{C_s^{MgO}} = \left(\frac{C_{s,exp}^{MgO} - C_{s,0}^{MgO}}{C_{T,exp}^{SiO_2} - C_{T,0}^{SiO_2}} \right) \bigg/ C_{s,0}^{MgO} \tag{6b}$$

To calculate γ for melt and solid densities we proceed in the same way:

$$\gamma_{\rho_m} = \left(\frac{\rho_{m,exp} - \rho_{m,0}}{C_{T,exp}^{SiO_2} - C_{T,0}^{SiO_2}} \right) \bigg/ \rho_{m,0} \tag{7a}$$
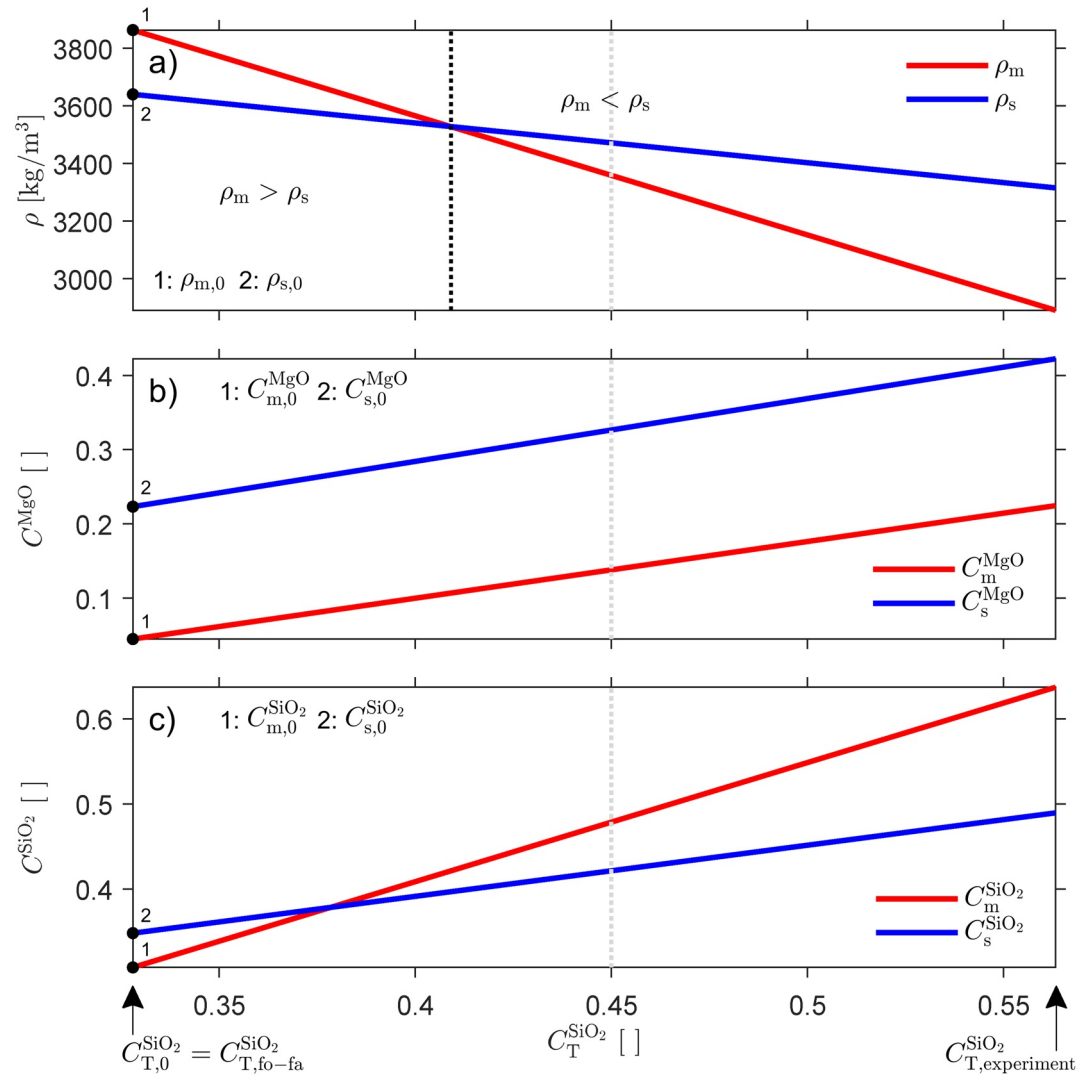
Figure 5. Linearized dependence of densities and mass fractions on total silica mass fraction, $C_T^{SiO_2}$. Panel (a) densities, melt in red and solid in blue, panel (b) mass fractions of magnesium, melt in red and solid in blue, and panel (c) mass fractions of silica, melt in red and solid in blue. Black points are reference values of each variable at T_0, P_0, and $C_{T,0}^{SiO_2}$ in Figure 4. $C_{T,experiment}^{SiO_2}$ corresponds to the total mass fraction of silica in the experiment of Davis et al. (2011). The black dashed line in panel (a) indicates at which total silica mass fraction the melt density becomes smaller than the solid density. The gray dashed line shows the value selected as the initial total silica mass fraction in the thermo-hydro-mechanical-chemical model.

$$\gamma_{\rho_s} = \left(\frac{\rho_{s,exp} - \rho_{s,0}}{C_{T,exp}^{SiO_2} - C_{T,0}^{SiO_2}} \right) \Big/ \rho_{s,0} \qquad (7b)$$

The values for the melt and solid densities, $\rho_{m,exp}$ and $\rho_{s,exp}$, are not provided in Davis et al. (2011). We calculate these densities using Holland and Powell's (1998) data base and the mineral mode reported in Table 1 of Davis et al. (2011) (see Appendix D for the detail of these calculations).

Figure 5 shows the linear variation for the different variables between the forsterite-fayalite binary olivine system, $C_{T,0}^{SiO_2} = 0.33$, and the experiment of Davis et al. (2011), $C_{T,experiment}^{SiO_2} = 0.56$, using the calculated values of γ. Figure 5a shows the relative change of solid and melt densities and the value of $C_T^{SiO_2} = 0.41$, indicated by the vertical black dashed line, for which melt and solid densities are equal.

To calculate the melt and solid thermal energies, U_m and U_s, required for the temperature calculation, we only consider, for simplicity, their variation with respect to temperature and density. We use values for the respective

melt and solid specific heat at the reference point T_0 and P_0, $C_{p_{m,0}}$ and $C_{p_{s,0}}$ (Table 2) and calculate the thermal energies by:

$$U_m = \rho_m \cdot c_{p_{m,0}} \cdot T \tag{8a}$$

$$U_s = \rho_s \cdot c_{p_{s,0}} \cdot T \tag{8b}$$

We apply this simplification of the thermal solid and melt energies because in our model the temperature deviation from the initial thermal gradient is small and we remain in the region of coexistence of melt and solid.

2.2. Thermo-Hydro-Mechanical-Chemical Transport Model

The applied THMC model is based on a system of conservation equations. The general derivation of these conservation equations is given in Appendix A and below only the applied equations are given. There are two fundamental approaches to include reactions in the mass conservation equations. One approach is to add source terms to the mass conservation equations, which are often called mass or volume transfer rate (e.g., McKenzie, 1984; Jones & Katz, 2018; see also Appendix B). The second approach, applied here, is to sum up the mass balances of each component over all possible phases resulting in the absence of any reaction-related source terms in the mass conservation equations (e.g., Beinlich et al., 2020; Orr, 2007; Plümper et al., 2016; Schmalholz et al., 2020). The conservation of total mass is

$$\frac{\partial}{\partial t}(\rho_m \varphi + \rho_s(1-\varphi)) = -\frac{\partial}{\partial x}(\rho_m \varphi v_m + \rho_s(1-\varphi)v_s) \tag{9}$$

where t is the time, φ is the porosity, x is the spatial coordinate (here the direction parallel to gravity), and v_m and v_s are the melt and solid velocity, respectively. The equation of conservation of total mass of MgO is

$$\frac{\partial}{\partial t}\left(C_m^{MgO}\rho_m \varphi + C_s^{MgO}\rho_s(1-\varphi)\right) = -\frac{\partial}{\partial x}\left(C_m^{MgO}\rho_m \varphi v_m + C_s^{MgO}\rho_s(1-\varphi)v_s\right) \tag{10}$$

and of conservation of total mass of SiO_2 is

$$\frac{\partial}{\partial t}\left(C_m^{SiO_2}\rho_m \varphi + C_s^{SiO_2}\rho_s(1-\varphi)\right) = -\frac{\partial}{\partial x}\left(C_m^{SiO_2}\rho_m \varphi v_m + C_s^{SiO_2}\rho_s(1-\varphi)v_s\right) \tag{11}$$

For the conservation of the total masses of MgO and SiO_2, we consider only the advective part of the conservation equation because we assume that diffusion processes are much slower than advection processes. The chemical reactions are included in the THMC model via the densities and mass fractions which vary with varying P, T, and $C_T^{SiO_2}$ (see Section 2.1), and via the associated porosity changes.

The conservation of thermal energy is

$$\frac{\partial}{\partial t}(U_m \varphi + U_s(1-\varphi)) = -\frac{\partial}{\partial x}\left(U_m \varphi v_m + U_s(1-\varphi)v_s - \lambda_T \frac{\partial T}{\partial x}\right) \tag{12}$$

where $\lambda_T = (\lambda_m \varphi + \lambda_s(1-\varphi))$ and λ_m and λ_s are the thermal conductivity of melt and solid, respectively. The latent heat of melting and crystallization is included via the evolving porosity (melt fraction), even if the heat capacities of melt and solid phases are constant. The impact of temporal porosity changes on the evolution of the thermal energy is visible when expressing the time derivative on the left-hand side of Equation 12 with several terms by applying the product rule of differentiation assuming constant heat capacities (8): $\partial/\partial t(U_m \varphi + U_s(1-\varphi)) = \varphi C_{p_{m,0}}\partial \rho_m T/\partial t + (1-\varphi)C_{p_{s,0}}\partial \rho_s T/\partial t + \partial \varphi/\partial t(U_m - U_s)$. In the absence of solid deformation and melt flow, a rise of temperature would cause variations in densities and mass fractions which, in turn, would cause variations in porosity via Equation 10 for the mass conservation of MgO (see also Section 2.3 below). Hence, crystallization and melting will adjust the phase compositions to the new equilibrium values and latent heat would buffer the temperature rise. Therefore, melting and crystallization are included in model.

The conservation of linear momentum of the solid is given by

$$\frac{\partial \sigma_{xx}}{\partial x} = \rho_T g \tag{13}$$

where σ_{xx} is the total stress, $\rho_T = \rho_m\varphi + \rho_s(1-\varphi)$ is the total density and g is the gravitational acceleration. The total stress is given by

$$\sigma_{xx} = -P_T + \tau \tag{14}$$

where P_T is the total pressure (i.e., the mean stress) and τ is the deviatoric stress. The conservation of linear momentum of the fluid, also known as Darcy's law, is given by

$$\varphi(v_m - v_s) = -\frac{k\varphi^3}{\eta_m}\left(\frac{\partial P_m}{\partial x} + \rho_m g\right) \tag{15}$$

where k is the permeability coefficient in a Kozeny-Carman type model, η_m is the melt viscosity and P_m is the melt pressure. We use the melt pressure as thermodynamic pressure for the thermodynamic calculations (e.g., Llana-Fúnez et al., 2012). The system of equations is closed by two constitutive equations. The first equation is used to calculate the total pressure,

$$P_T = P_m - \frac{\partial v_s}{\partial x}(1-\varphi)\eta_v \tag{16}$$

where η_v is the solid bulk viscosity. We consider in the equation for P_T only a viscous volumetric deformation. However, effects of reversible elastic volumetric deformation are considered in our model via the compressibility, β, which quantifies the variation of densities caused by variations in P_m (Table 2 and Equation 3). These density variations are considered in the mass conservation equations and, hence, cause a volumetric deformation. Therefore, temporal variations in P_m can cause variations in volumetric deformation due to consideration of the compressibility, in a similar way as described by a standard equation for elastic volumetric deformation, such as $\beta\partial P_m/\partial t = -\partial v_s/\partial x$. Effects of reversible elastic volumetric deformation are, hence, considered in our THMC model by the consideration of reversible equilibrium reactions. The second constitutive equation is used to calculate τ by

$$\tau = 2\eta_s \frac{\partial v_s}{\partial x} \tag{17}$$

where η_s is the shear viscosity of the solid. For more details on the derivation of the equations, see Appendix A.

2.3. Coupled THMC and Thermodynamic Model and Numerical Method

The entire system of equations describing the THMC and thermodynamic models has a total of 14 unknowns: eight unknowns are determined by the thermodynamic model, namely ρ_m, ρ_s, C_m^{MgO}, C_s^{MgO}, $C_m^{SiO_2}$, $C_s^{SiO_2}$, U_m, and U_s, and six unknowns are determined by the THMC model, namely P_m, φ, $C_T^{SiO_2}$, T, v_m, and v_s. In the thermodynamic model, the unknowns are determined by T, P_m, and $C_T^{SiO_2}$ using pre-computed results from Gibbs energy minimizations (i.e., phase diagrams of the eight thermodynamic variables; Figures 4 and 5). In the THMC model, the unknowns are calculated by numerically solving a system of coupled partial differential equations.

We use a standard staggered grid finite difference (FD) method (e.g., Gerya, 2019) to solve the partial differential equations of the THMC model. The numerical algorithm consists of a standard time loop with an internal pseudo-transient (PT) iterative loop to determine P_m, φ, $C_T^{SiO_2}$, T, and v_s. This PT method (e.g., Duretz et al., 2019; Räss et al., 2019; Schmalholz et al., 2020) solves non-linear system of equations in an iterative way without the need of linearization and solving a large system of linear algebraic equations. To use the PT method, we transform the conservation equations in PT equations by adding a PT time derivative, with PT time step Δt^{PT}, for each unknown variable, P_m, φ, $C_T^{SiO_2}$, T, and v_s. The PT equations are

$$\frac{\Delta P_m}{\Delta t_P{}^{TP}} = -\frac{\partial}{\partial t}(\rho_m\varphi + \rho_s(1-\varphi)) - \frac{\partial}{\partial x}\left(-\rho_m\frac{k\varphi^3}{\eta_m}\left(\frac{\partial P_m}{\partial x} + \rho_m g\right) + \rho_T v_s\right) \tag{18a}$$

$$\frac{\Delta \varphi}{\Delta t_\varphi{}^{TP}} = -\frac{\partial}{\partial t}\left(C_m^{MgO}\rho_m\varphi + C_s^{MgO}\rho_s(1-\varphi)\right) - \frac{\partial}{\partial x}\left(C_m^{MgO}\rho_m\varphi v_m + C_s^{MgO}\rho_s(1-\varphi)v_s\right) \tag{18b}$$

$$\frac{\Delta C_T^{SiO_2}}{\Delta t_{C_T^{SiO_2}}{}^{TP}} = -\frac{\partial}{\partial t}\left(C_m^{SiO_2}\rho_m\varphi + C_s^{SiO_2}\rho_s(1-\varphi)\right) - \frac{\partial}{\partial x}\left(C_m^{SiO_2}\rho_m\varphi v_m + C_s^{SiO_2}\rho_s(1-\varphi)v_s\right) \tag{18c}$$

$$\frac{\Delta T}{\Delta t_{\mathrm{T}}{}^{\mathrm{TP}}} = -\frac{\partial}{\partial t}\left(U_{\mathrm{m}}\varphi + U_{\mathrm{s}}\left(1-\varphi\right)\right) - \frac{\partial}{\partial x}\left(U_{\mathrm{m}}\varphi v_{\mathrm{m}} + U_{\mathrm{s}}\left(1-\varphi\right)v_{\mathrm{s}} - \lambda_{\mathrm{tot}}\frac{\partial T}{\partial x}\right) \tag{18d}$$

$$\frac{\Delta v_{\mathrm{s}}}{\Delta t_{v_{\mathrm{s}}}{}^{\mathrm{TP}}} = \frac{\partial}{\partial x}\left(-P_{\mathrm{T}} + \tau\right) - \rho_{\mathrm{T}}g \tag{18e}$$

When the PT time derivatives on the left-hand sides of the equations above are zero, the corresponding equations of the right-hand side are solved. In practice, the PT iteration will continue until all PT time derivatives are smaller than a specified numerical tolerance error. In the FD method, we use numerical time steps representing the physical time step Δt to approximate the time derivatives, which control the physical time evolution (i.e., the "real" time derivatives). We employ five PT time steps to solve for P_{m}, $\Delta t_{\mathrm{P}}{}^{\mathrm{TP}}$, for φ, $\Delta t_{\varphi}{}^{\mathrm{TP}}$, for $C_{\mathrm{T}}^{\mathrm{SiO_2}}$, $\Delta t_{C_{\mathrm{T}}^{\mathrm{SiO_2}}}{}^{\mathrm{TP}}$, for T, $\Delta t_{\mathrm{T}}{}^{\mathrm{TP}}$, and for v_{s}, $\Delta t_{v_{\mathrm{s}}}{}^{\mathrm{TP}}$. The choice of these numerical PT time steps is crucial for a stable convergence of the PT iterative solution but does not affect the result after the convergence. The values of the PT time steps are given in Appendix C, Table C1. The melt velocity can be directly calculated from Darcy's law (Equation 15), which does not require the solution of an additional differential equation.

2.4. Model Configuration and Characteristic Values

In the numerical algorithm, we use the same equations with the same model parameters as presented in Sections 2.2 and 2.3. However, before the actual numerical calculations, we non-dimensionalize the model parameters and variables. For the nondimensionalization, we choose four independent characteristic scales: (a) the reference melt density times gravitational acceleration, $\rho_{\mathrm{m,0}}g$ (Pa·m^{-1}), (b) the permeability divided by melt viscosity, k/η_{m} (m^2·Pa^{-1}·s^{-1}), (c) the solid bulk viscosity, η_{v} (Pa·s), and (d) half the temperature difference across the model, ΔT^{A} (K). All model parameters and variables are scaled by these four characteristic scales. The characteristic scales are themselves model parameters which are scaled, so that practically these four characteristic scales are set to 1 in the numerical algorithm (see numerical algorithm which is provided as Supporting Information S1). With these independent characteristic scales, we can determine the dependent characteristic length, $L_{\mathrm{c}} = \sqrt{\frac{k}{\eta_{\mathrm{m}}}\cdot\eta_{\mathrm{v}}}$ (m) of the model. L_{c} is also known as compaction length in the context of porosity waves (e.g., Connolly & Podladchikov, 2007; McKenzie, 1985), which corresponds to the characteristic distance over which compaction occurs. Next, we define several dimensionally dependent spatial scales to configure the model. These spatial scales must be chosen in such way that the considered compaction-driven melt migration can be numerically resolved. We consider initial spatial distributions of porosity and/or total concentration of SiO$_2$ that have the form of a Gaussian with a standard deviation, or width w, which is 10 times larger than the compaction length, $w = 10\cdot L_{\mathrm{c}}$, so that the applied distribution can initiate a significant compaction-driven melt migration (e.g., Dohmen & Schmeling, 2021). If $w \ll L_{\mathrm{c}}$ then the distributions of porosity and/or total concentration of SiO$_2$ will not initiate a significant compaction-driven melt flow by porosity waves (e.g., Dohmen & Schmeling, 2021). To be able to model a significant distance of melt migration we apply a model height $Lx = 100\cdot L_{\mathrm{c}}$.

The relation between solid and melt densities is determined by the thermodynamic results (Table 2) and $\rho_{\mathrm{s,0}}g = (\rho_{\mathrm{s,0}}/\rho_{\mathrm{m,0}})\cdot\rho_{\mathrm{m,0}}g = 0.9423\cdot\rho_{\mathrm{m,0}}g$. Next, we configure four initial profiles for temperature, porosity, total concentration of SiO$_2$ and total pressure (Figure 6). First, we apply a constant porosity with a value of 0.02 and a constant total concentration of SiO$_2$ with a value of 0.45 (in Figure 5 this silica mass fraction corresponds to the gray dashed lines in the region where melt density is lower than solid density). We then add a perturbation to the porosity and/or the total silica mass fraction in the form of a Gaussian with $w = 10\cdot L_{\mathrm{c}}$ and with its maximum value at a depth of $x = -20\cdot L_{\mathrm{c}}$ (Figures 6g and 6h). For the simulations presented below, we apply five perturbation amplitudes, or heights of the Gaussian distribution, for porosity, $\Delta\varphi$ (0.005, 0.01, 0.02, 0.03, and 0.04) and five for total silica mass fraction, $\Delta C_{\mathrm{T}}^{\mathrm{SiO_2}}$ (0, 0.25, 0.5, 0.75, and 1; see Figure 7 for the systematic scheme of the simulations). We define the temperature profile in the model with a temperature difference $\Delta T_{\mathrm{model}} = 2\cdot\Delta T^{\mathrm{A}}$ between the bottom and the top of our model (Figure 6d). For the initial total pressure profile, we calculate the lithostatic pressure across the model with the total densities and obtain a pressure difference $\Delta P_{\mathrm{model}}$ of approximately $90\cdot P_{\mathrm{c}}$ ($P_{\mathrm{c}} = \rho_{\mathrm{m,0}}g\cdot L_{\mathrm{c}}$) for all simulations.

Next, we specify that our model represents a natural region in which the pressure increases from top to bottom by 1 (GPa), that is $\Delta P_{\mathrm{nature}} = 1$ (GPa). This pressure range corresponds to the pressure range chosen for the thermodynamic data (Figure 4). We then determine the vertical distance, h, necessary to obtain a pressure increase of 1 (GPa) with $h = P/(\rho_{\mathrm{T}}g)$, using $\rho_{\mathrm{T}} = \rho_{\mathrm{m,0}}\varphi + \rho_{\mathrm{s,0}}(1-\varphi)$ and $\varphi = 0.02$. For the applied parameters, $h \approx 28$ (km). This means that our model height of $Lx = 100\cdot L_{\mathrm{c}}$ represents a natural mantle region with a height of ≈ 28 (km).
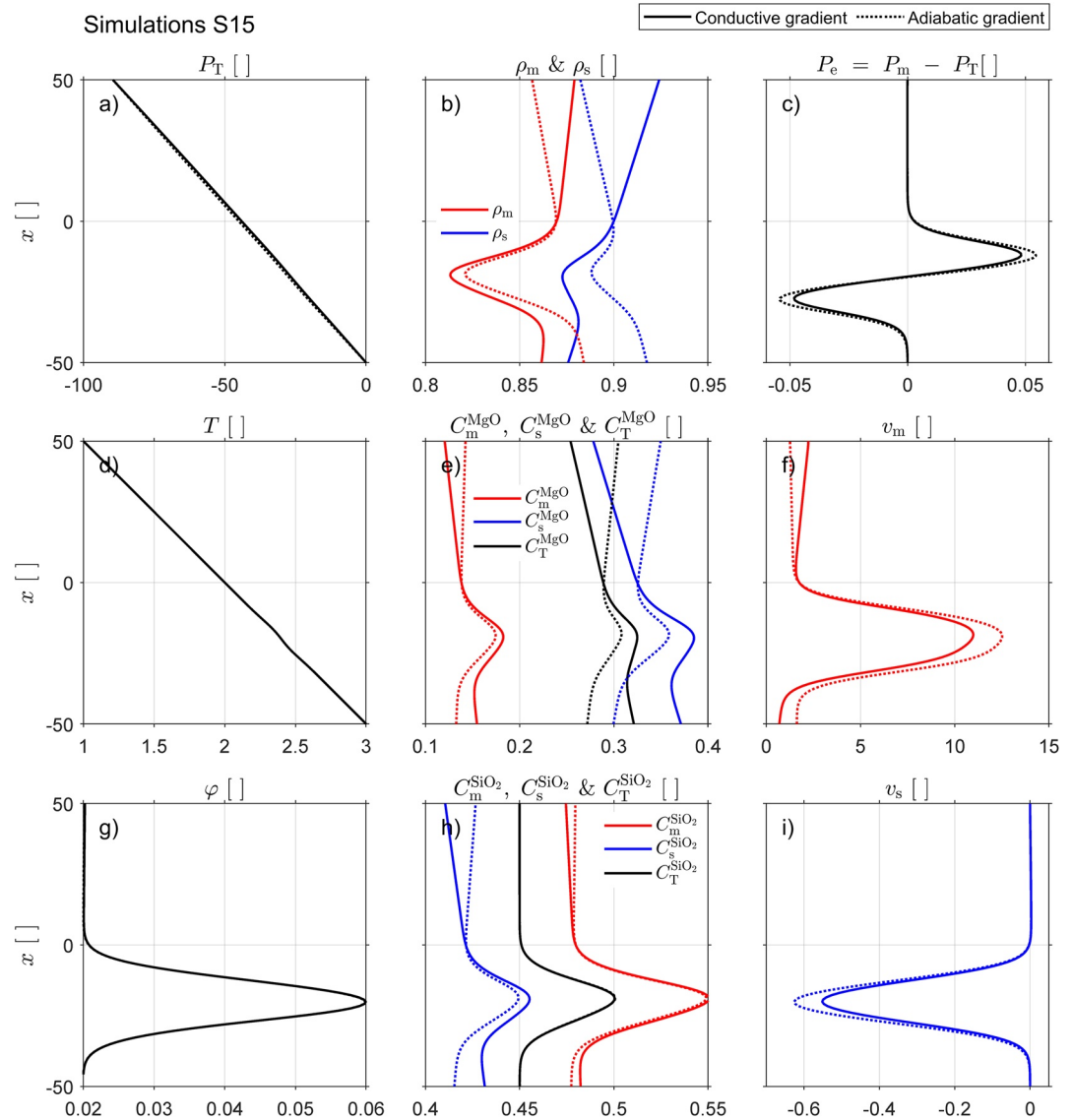
Figure 6. Initial profiles for simulation S15 for a conductive gradient (solid lines) and for an adiabatic gradient (dashed lines). All variables are dimensionless. Panel (a) shows total pressure. Panel (b) shows melt density (red lines) and solid density (blue lines). Panel (c) shows effective pressure, positive values indicate decompaction while negative values indicate compaction. Panel (d) shows temperature. Panel (e) shows magnesium mass fraction in melt (red lines) and in solid (blue lines) and total magnesium mass fraction (black lines). Panel (f) shows melt velocity. Panel (g) shows porosity. Panel (h) shows silica mass fraction in melt (red lines) and in the solid (blue lines) and total silica mass fraction (black lines). Panel (i) shows solid velocity.

We performed two series of systematic simulations with two different thermal gradients, one representing an adiabatic and one a conductive gradient. A typical adiabatic temperature gradient is between 0.5 and 0.55 (°C·km^{-1}). Therefore, we assume a natural temperature difference of $\Delta T_{\text{nature,1}} = 15$ (K) (subscript 1 indicates the adiabatic gradient) across a natural region with $h \approx 28$ (km) to represent a region with adiabatic gradient. A conductive temperature gradient is typically an order of magnitude larger than the adiabatic gradient. Hence, we consider that $\Delta T_{\text{nature,2}} = 150$ (K) (subscript 2 indicates the conductive gradient) across a natural region with $h \approx 28$ (km) represents a region with a conductive gradient. The exact value of $\Delta T_{\text{nature,2}}$ is not important for our model, however, the important effect is that for the applied two temperature differences the variation of densities with depth is fundamentally different, as will be shown in results of Section 3.1. Once the natural pressure and temperature differences are specified, we can rescale the calculated values of α and β (Table 2) to the model configuration
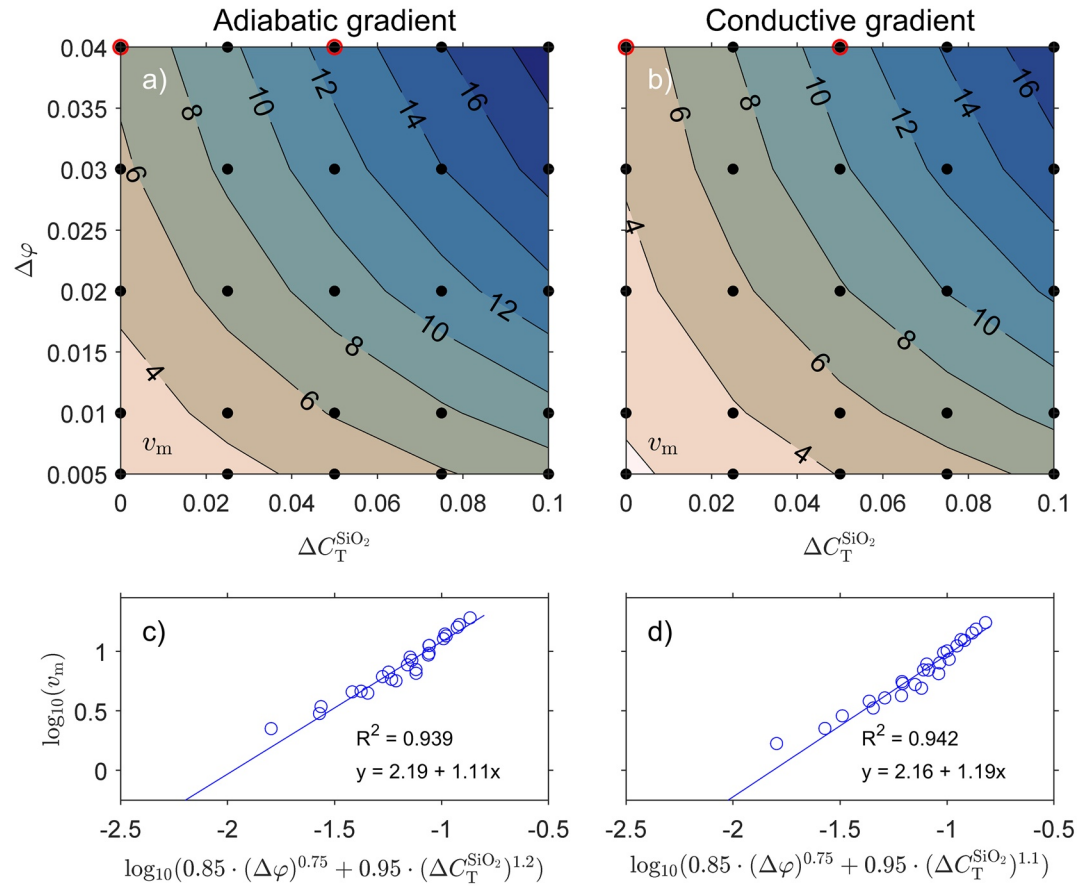
Figure 7. Panels (a) and (b) show maximal initial melt velocities as function of initial porosity, $\Delta\varphi$, and total silica mass fraction, $\Delta C_T^{SiO_2}$, perturbation amplitudes. (a) For adiabatic gradient and (b) for conductive gradient. Black lines show the velocity contours and red circles indicate the initial perturbations for four simulations for which the time evolution has been calculated: simulations S05 (top left in panels (a) and (b)) and S15 (top in the middle in panels (a) and (b)) for both temperature gradients. Panels (c) and (d) show the power low relationship between melt velocity and a combination of porosity and total silica mass fraction perturbation amplitude, (c) for adiabatic gradient and (d) for conductive gradient. In panels (c) and (d), blue points represent the 25 systematic simulations and the blue line the linear regression line.

using, respectively, a temperature ratio ($\Delta T_{nature}/\Delta T_{model}$) and a pressure ratio ($\Delta P_{nature}/\Delta P_{model}$). Since the values of ΔP_{model} and ΔT_{model} are defined by characteristic values (see above), their specific values in the numerical algorithms are 90 and 2, respectively.

Finally, all remaining parameters are specified with respect to the independent parameters. For simplicity, we set the shear viscosity equal to the bulk viscosity $\eta_s = \eta_v$. Concerning the thermal parameters, we divide the equation for thermal energy (Equation 18d) by $\rho c_{p_{m,0}}$ so that in this equation the thermal parameters reduce from three to two: $\rho c_{p_{s,0}}/\rho c_{p_{m,0}}$ and $\lambda_m/\rho c_{p_{m,0}}$. The ratio $\rho c_{p_{s,0}}/\rho c_{p_{m,0}} = \rho_{s,0}/\rho_{m,0} \cdot c_{p_{s,0}}/c_{p_{m,0}}$ and is determined by values from Table 2. To determine a reasonable value for the scaled thermal diffusivity, $\lambda_m/\rho c_{p_{m,0}}$, we consider a Peclet number, $P_e = v_c \cdot L_c \cdot \rho c_{p_{m,0}}/\lambda_m$, where the characteristic velocity $v_c = L_c/t_c = k \cdot \rho_{m,0}g/\eta_m$, using the characteristic time $t_c = \eta_v/\rho_{m,0}g \cdot L_c$. The Peclet number can be reformulated to $P_e = \frac{\rho_{m,0}g \cdot L_c^3}{\eta_v} \cdot \frac{\rho c_{p_{m,0}}}{\lambda_m}$. The scaled value for the thermal diffusivity is then given by $\frac{\lambda_m}{\rho c_{p_{m,0}}} = \frac{\rho_{m,0}g \cdot L_c^3}{\eta_v \cdot P_e}$. Values of P_e typical for our application of melt migration around the LAB are in the order of 1, for example, by using $\rho_{m,0}g \approx 37,896$ (Pa·m^{-1}; Table 2), $L_c \approx 1$ (km), $\eta_v \approx 6 \times 10^{19}$ (Pa·s), $\rho c_{p_{m,0}} \approx 4,821,024$ (J·K^{-1}·m^{-3}) (Table 2), and $\lambda_m \approx 3$ (W·K^{-1}·m^{-1}). We, hence, consider a value of $P_e = 1$ for our simulations and because the scaled thermal diffusivity depends only on the applied characteristic scales and P_e its value in the numerical algorithm is 1. The model results presented below can be rescaled to different natural situations and parameters by applying the characteristic scales and natural parameters mentioned above (see Section 4).

3. Results

We first present results from the thermodynamic model which consist essentially of the determined values of α, β, and γ for the thermodynamic variables (Table 2). Subsequently, we show results from the THMC melt migration model.

3.1. Linearization of Thermodynamic Results

The calculated values of all α, β, and γ are presented in Table 2. The determined values of α, β, and γ provide a transparent overview on the relative importance and interdependence of the parameters. For example, the α for solid density $^{\alpha}\rho_s$ and for solid mass fraction of silica $\alpha_{C_s^{SiO_2}}$ are 2–5 times larger than values of α for melt density $^{\alpha}\rho_m$ and for melt mass fraction of silica $\alpha_{C_m^{SiO_2}}$. This relationship is opposite for magnesium mass fraction where α for the melt, $\alpha_{C_m^{MgO}}$, is 1.5 times larger than the one for the solid, $\alpha_{C_s^{Mgo}}$. We observe the same trend for β, where β_{ρ_s} and $\beta_{C_s^{SiO_2}}$ are 1.5–4 times larger than $^{\beta}\rho_m$ and $\beta_{C_m^{SiO_2}}$ and $\beta_{C_m^{MgO}}$ is slightly larger than $\beta_{C_s^{MgO}}$. For the γ the situation is different, because all γ values for melt ($^{\gamma}\rho_m$, $\gamma_{C_m^{MgO}}$, and $\gamma_{C_m^{SiO_2}}$) are 2.5–4.5 times larger than γ values for solid ($^{\gamma}\rho_s$, $\gamma_{C_s^{MgO}}$, and $\gamma_{C_s^{SiO_2}}$). The difference in dependence on P, T, and $C_T^{SiO_2}$ between variables related to melt and solid is between a factor of 1.5 and 4.5 and it is, hence, important to consider this difference in the THMC model.

The initial density profile of the model impacts the melt migration. For a constant chemical composition, the initial density profile is controlled by the initial variation of P and T, but with opposite trend: from the top to the bottom of the model, the melt and solid densities increase with increasing pressure but decrease with increasing temperature. We determine for the applied values of ΔT and ΔP the critical value of ΔT, for which the density is constant with depth. We use the equation

$$\rho = \rho_0 \left(1 + \alpha \Delta T + \beta \Delta P\right) \tag{19}$$

and reformulate the equation to

$$\frac{\Delta\rho}{\rho_0\alpha} = \Delta T + \frac{\beta}{\alpha}\Delta P \tag{20}$$

where $\Delta\rho = \rho - \rho_0$. We assume no density variation (isochoric system) with a variation of T and P, that is, $\Delta\rho/\alpha = 0$ and solve the remaining equation for ΔT which yields

$$\Delta T = -\frac{\beta}{\alpha}\Delta P \tag{21}$$

If the applied ΔT is larger than the expression above, then the density is decreasing with depth in the model (i.e., the initial density variation is controlled by the temperature variation). If ΔT is smaller, then the density increases with depth, controlled by the pressure increase with depth. The above analysis can also be applied to the mass fractions. Choosing ΔP of 1 (GPa) and using α and β values from Table 2, we obtain for the melt density a critical $\Delta T = 98.2$ (K), for the solid density a critical $\Delta T = 72.5$ (K), for magnesium melt mass fraction a critical $\Delta T = 45.3$ (K), for magnesium solid mass fraction a critical $\Delta T = 63.2$ (K), for silica melt mass fraction a critical $\Delta T = 45.6$ (K), and for silica solid mass fraction a critical $\Delta T = 62.6$ (K). All values of critical ΔT are between $\Delta T_{nature,1}$ and $\Delta T_{nature,2}$, respectively, that is the temperature differences applied for the adiabatic and the conductive gradient. Therefore, the applied initial adiabatic and conductive geotherms cause a fundamentally different variation of densities and mass fractions with depth: for a conductive geotherm, densities and mass fractions decrease with depth and for an adiabatic gradient they increase with depth (Figure 6).

3.2. THMC Model Results: Comparison of Initial Profiles, Maximum Melt Velocity and Evolution Over Time

We performed 50 simulations with five time steps only to determine the initial profiles of all the involved model variables, because the initial profiles of, for example, the solid and melt velocities represent already an interesting result that needs to be calculated iteratively due to the nonlinear coupling of the model variables. For four of these simulations, we also calculate the evolution with time to investigate the upward melt migration by reactive porosity waves.

3.2.1. Comparison of Initial Profiles

We first compare initial profiles from four different simulations, namely simulations termed S05 with an initial porosity perturbation only (Figure C1) and simulations S15 with an initial porosity and total silica mass fraction perturbations (Figure 6), both for the two temperature gradients, namely a conductive gradient (solid lines in Figures 6 and C1) and an adiabatic gradient (dashed lines in Figures 6 and C1). The four simulations show similar profiles for total pressure (Figure 6a), effective pressure, $P_e = P_m - P_T$ (Figure 6c), temperature (Figure 6d), porosity (Figure 6g), and solid velocity (Figure 6i). The effective pressure shows which part of the model is in compression (P_e is negative) and which part is in dilation (P_e is positive). The main difference between the four simulations is the maximum magnitudes of the peaks of the corresponding profiles of the model variables. Maximum magnitudes are larger in the two S15 simulations (Figure 6), with an initial perturbation in porosity and in total silica mass fraction, than in the two S05 simulations (Figure C1), with an initial perturbation only in porosity. Differences between the four simulations are visible in the calculated profiles of densities (Figure 6b), of magnesium and silica mass fractions (Figures 6e and 6h) and of melt velocity (Figure 6f). There is a significant difference between simulations with a conductive gradient (solid lines in Figures 6 and C1) and simulations with an adiabatic gradient (dashed lines in Figures 6 and C1). Across the model, density profiles for the conductive gradient (solid lines in panel b in Figures 6 and C1) decrease with increasing depth, whereas for the adiabatic gradient (dashed lines in panel b in Figures 6 and C1), densities increase with increasing depth, as predicted in Section 3.1. This trend is reversed for melt and solid mass fraction of magnesium and silica (panels e and h in Figures 6 and C1). For the conductive gradient, melt and solid mass fraction of magnesium and silica increase with increasing depth and with the adiabatic gradient, melt and solid mass fraction of magnesium and silica decrease with increasing depth. The calculated total magnesium mass fraction (black lines in panel e in Figures 6 and C1) follows the trend of melt and solid mass fractions of magnesium. The calculated total silica mass fraction (black lines in panel h in Figures 6 and C1) remains constant except in the region of the perturbation where the maximum value changes according to the applied initial perturbations. The melt velocity profiles (panel f in Figures 6 and C1) exhibit the maximum melt velocity at the position where the maximum initial perturbation in porosity and/or total silica mass fraction is applied. The maximum melt velocity is greater when both porosity and total silica mass fraction profiles exhibit initial perturbations (simulation S15, Figure 6). The initial melt velocity profile shows positive values indicating upward motion of the melt (Figures 6 and C1, panel e), while the solid velocity is negative indicating compaction in the region where the melt is moving upward, or where melt is extracted (Figures 6 and C1, panel i). Also, the absolute magnitudes of the melt velocities around the maximal initial perturbation are approximately one order of magnitude larger than absolute magnitudes of the solid velocities.

3.2.2. Comparison of Maximum Melt Velocity

Figure 7 compares maximum melt velocities of the respective initial profiles for 50 simulations. We made 25 simulations with an adiabatic gradient (Figures 7a) and 25 simulations with a conductive gradient (Figure 7b). For each thermal gradient, we applied 5 perturbation amplitudes for the initial porosity, $\Delta\varphi$, and 5 amplitudes for the initial total silica mass fraction, $\Delta C_T^{SiO_2}$. The four simulations selected for investigating the time evolution, that is, S05 and S15, are represented by the points circled in red (Figure 7). The greater the amplitudes of the perturbations, the greater the maximum melt velocity. The maximum melt velocity occurs when both perturbation amplitudes are maximal, which applies for both thermal gradients. The rise of initial porosity increases the effective permeability and hence the melt velocity is larger for larger porosity. The rise in initial silica increases the initial density difference and hence increases the melt velocity. The maximal melt velocities are slightly larger for an adiabatic gradient (Figure 7). The maximal value of the effective pressure in simulation S15 is slightly smaller for the conductive gradient (solid line in Figure 6c) than for the adiabatic gradient (dashed line in Figure 6c). Therefore, the velocities are larger for an adiabatic gradient. However, the effective pressure is a result of the interplay between buoyancy-driven non-linear hydraulics and viscous compaction, and the melt velocity is, hence, the integrated and calculated result of these coupled processes. The curved velocity contours in Figure 7 indicate a nonlinear dependence between the maximal melt velocity and $\Delta\varphi$ and $\Delta C_T^{SiO_2}$. However, the 25 maximal melt velocities for each thermal gradient can be collapsed from the 2D space ($\Delta\varphi - \Delta C_T^{SiO_2}$) onto a 1D space (Figures 7c and 7d). The equations of this data collapse, or fit, are obtained by a linear best fit of the 25 data points and are given as label of the horizontal axis. The two best-fit equations show that the difference in maximal melt velocity for the two thermal gradients is only due to a different sensitivity to $\Delta C_T^{SiO_2}$, with exponents 1.1 and

1.2, because the exponents of $\Delta\varphi$ are identical for the two thermal gradients (Figures 7c and 7d). Overall, for the chosen parameters, a perturbation in total silica mass fraction has a similar impact on the maximal melt velocity as a perturbation in the initial porosity.

3.2.3. Time Evolution and Reactive Porosity Wave Propagation

Figure 8 shows the time evolution of the S15 simulation with a conductive gradient. The additional Figures C2–C4 show the three other simulations, namely S05 with a conductive gradient, and S05 and S15 with an adiabatic gradient. The evolution of porosity (Figure 8a) and of effective pressure (Figure 8b) corresponds to a typical evolution of 1D porosity waves (e.g., Connolly & Podladchikov, 2013; Jordan et al., 2018). Hence, the simulations show that the developed THMC model is able to generate upward-traveling porosity waves. During porosity wave propagation, the maximum porosity always corresponds to an effective pressure of zero (Figures 8a and 8b). The compaction at the base of the high porosity region (where P_e is minimum) allows the melt to rise upward into the high porosity region under decompaction (where P_e is maximum). Comparing all porosity profiles (Figures 8a and C2–C4) for the two S05 simulations (Figures C2 and C3), the maximum porosity decreases slightly with progressive time and then remains constant, whereas for the two S15 simulations (Figures 8 and C4), the maximum porosity increases and then decreases slightly. The two simulations with an adiabatic gradient (Figure C3 for S05 and Figure C4 for S15) show a stabilization of the maximum melt velocity over time, while the two simulations with a conductive gradient (Figure C2 for S05 and Figure 8 for S15) show a slight increase in melt velocity over time. For the four simulations (Figures 8 and C2–C4), the variations of melt density and total silica mass fraction are small over time compared to the total magnesium mass fraction which show a slightly greater variation, especially for simulations with an adiabatic gradient (Figures C3 and C4).

Figure 9 shows the time evolution of the melt density (panel a), the total magnesium mass fraction (panel b), and the total silica mass fraction (panel c) at depth $x = 10$ ( ) for the four simulations. The variation in melt density (Figure 9a) for the two S05 simulations (conductive in light blue and adiabatic in gray) and the two S15 simulations (conductive in dark blue and adiabatic in black) is very similar. The main difference is the magnitude of the initial value at time $t = 0$ for the two different thermal gradients. The initial value for the conductive gradient is larger than the initial value for the adiabatic gradient (ρ_m of S05 and S15 conductive $> \rho_m$ of S05 and S15 adiabatic). Similar variations are observed for total magnesium mass fraction (panel b) for the two S05 simulations (conductive in light blue and adiabatic in gray) and the two S15 simulations (conductive in dark blue and adiabatic in black). For melt density, the magnitude of the initial value at time $t = 0$ between the two thermal gradients are different. The initial value for the adiabatic gradient is larger than the initial value for the conductive gradient (C_T^{MgO} of S05 and S15 adiabatic $> C_T^{MgO}$ of S05 and S15 conductive). For the variation of the total silica mass fraction (panel c), the initial value is identical for all four simulations since this value is specified as initial condition. The local variation of the total silica mass fraction over time is larger than the initial value (at $t = 0$) for the simulations with an adiabatic gradient (black and gray lines) and is smaller for the simulations with a conductive gradient (dark and light blue lines). The maximum peaks of the two S15 simulations (black and dark blue lines) arrive before the maximum peaks of the two S05 simulations (gray and light blue lines). This is consistent with the fact that S15 simulations have a greater initial perturbation, hence the melt velocity is larger and the maximum peaks arrive first.

4. Discussion

4.1. Mobility and Mass Transport

In the modeled chemical system, the mass fractions of MgO and SiO_2 in the melt and solid are variable and are functions of pressure, temperature and total silica content. Our model can be considered as fully mobile since there are no restrictions on the mobility of MgO and SiO_2 so that MgO and SiO_2 can be freely exchanged between solid and melt. This full mobility is an elaboration compared to existing studies on reactive transport with fluid-rock interactions, who assume that some chemical components are immobile and fixed to the solid phase (e.g., Beinlich et al., 2020; Plümper et al., 2016). Furthermore, in our model the total mass of MgO and SiO_2 can locally change permanently due to mass transport by melt migration. In contrast, other studies on melt migration with chemical differentiation consider the silica mass fraction as a function of temperature only (e.g., Jackson et al., 2018). Therefore, for a given temperature the silica mass fraction cannot change by transport. In our model, the mobility and mass transport are enabled by a freely evolving porosity, which is calculated from
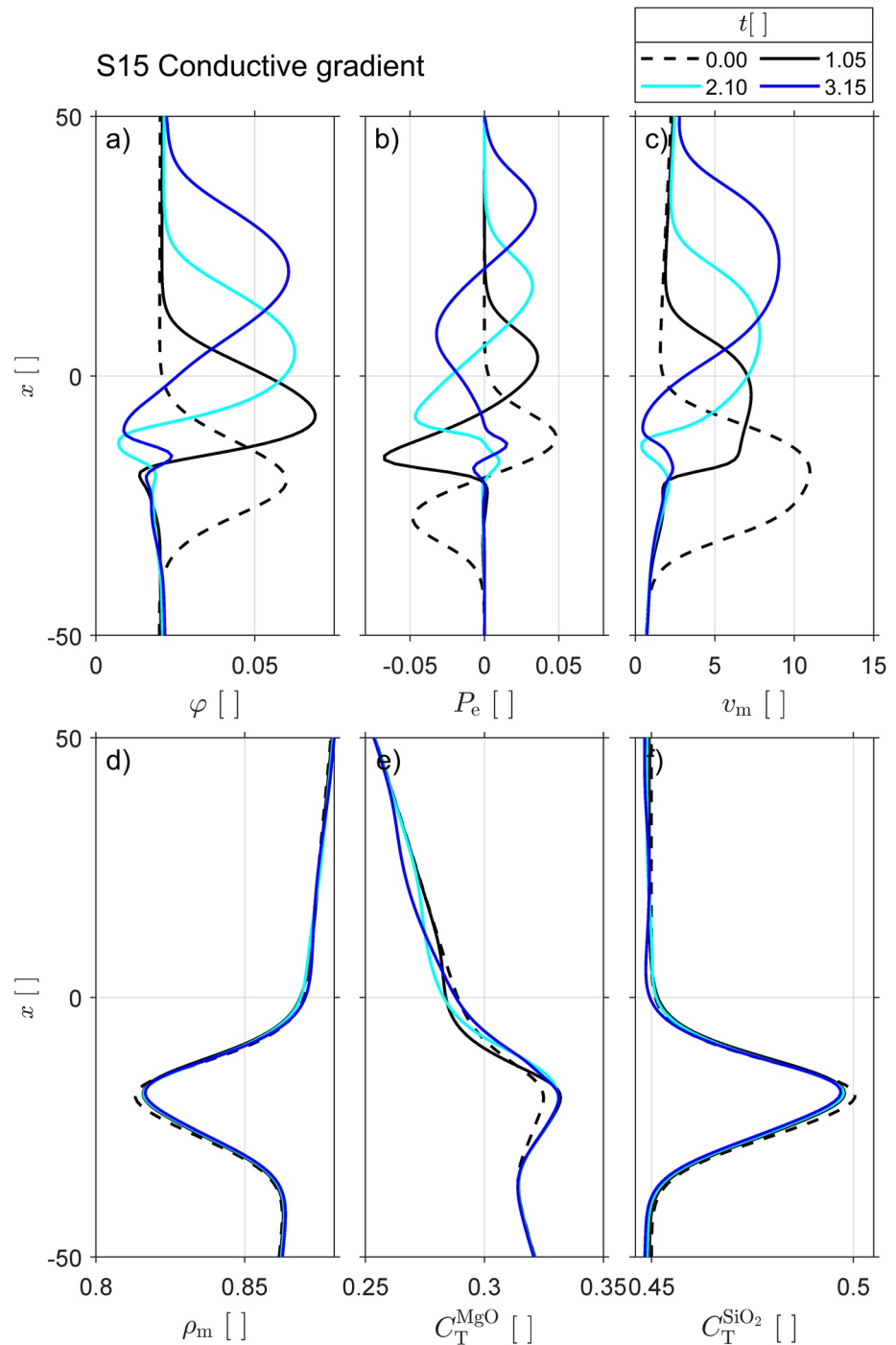
Figure 8. Time evolution of six variables for simulation S15 with conductive gradient; all variables are dimensionless. Panel (a) shows porosity, panel (b) shows effective pressure, panel (c) shows melt velocity, panel (d) shows melt density, panel (e) shows total magnesium mass fraction, and panel (f) shows total silica mass fraction. Four time steps are chosen at different dimensional times: $t = 0$ with dashed line (corresponding to the initial profiles, solid lines, in Figure 6 for each variable), $t = 1.05$ with black line, $t = 2.10$ with light blue, and $t = 3.15$ with dark blue (see legend). The dimensionless time can be scaled to a physical time using the characteristic time scale $t_c = \frac{\eta_v}{\rho_{m,0} g \cdot L_c}$ (see Section 2.4).

the conservation equation for the total mass of MgO. For example, inside the considered partial melting region of the olivine phase diagram (Figure 3), the densities (Figure 3b) and mass fractions of MgO of solid and melt (Figure 3c) are fixed for a given temperature and pressure, independent on the composition X (Gibbs phase rule). The
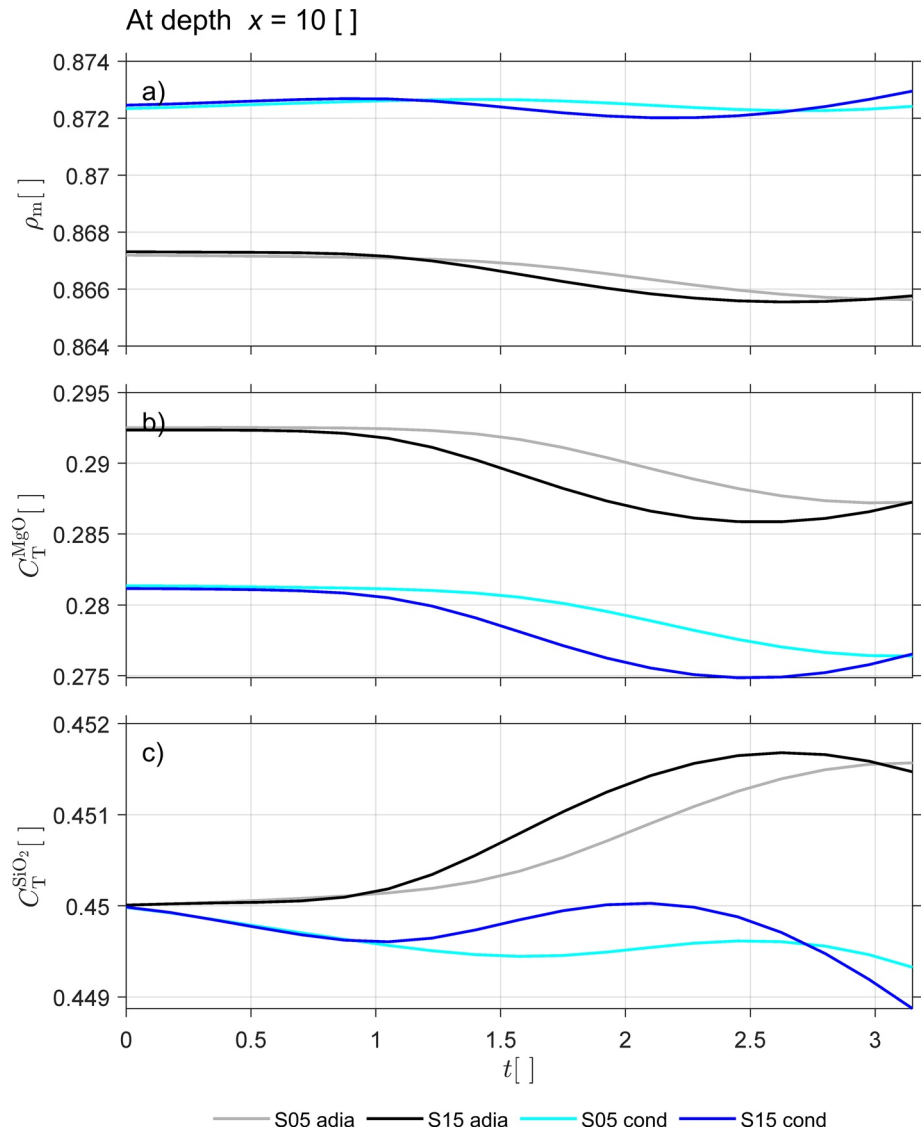
Figure 9. Time evolution, at a fixed depth of $x = 10$, of three variables for the four simulations indicated by red circles in Figure 7: simulation S05 for adiabatic gradient in gray, simulation S15 for adiabatic gradient in black, simulation S05 for conductive gradient in light blue and simulation S15 for conductive gradient in dark blue. All variables are dimensionless. Panel (a) shows melt density. Panel (b) shows total magnesium mass fraction and panel (c) shows total silica mass fraction.

total mass of MgO is calculated by the mass fractions, densities and porosity. If the total mass of MgO is locally modified due to an advective melt flux, and densities and mass fractions of MgO are fixed, then the porosity of the system must change to enable and balance the mass transport.

Melt, or mass, transport can be quantified by the transport of incompatible tracers inside the melt (e.g., Jordan et al., 2018). The conservation equation for such incompatible tracer, having a concentration C_m^{Tr} in the melt, is

$$\frac{\partial \left(C_m^{Tr} \rho_m \varphi \right)}{\partial t} + \frac{\partial}{\partial x} \left(C_m^{Tr} \rho_m \varphi \upsilon_m \right) = 0 \tag{22}$$

We model the evolution of such tracer and consider an initial profile of C_m^{Tr} which has the same Gaussian shape as the initial profiles of φ and $C_T^{SiO_2}$ but having a maximal value of one. We calculate the evolution of C_m^{Tr} applying the PT method to the conservation equation for the tracer during the simulations. Simulation S15 shows that the porosity wave (Figure 10a) propagates with a slightly faster velocity compared to the velocity of the tracer (Figure 10b). This velocity difference is manifested in the different position of the maximal values of φ and of the
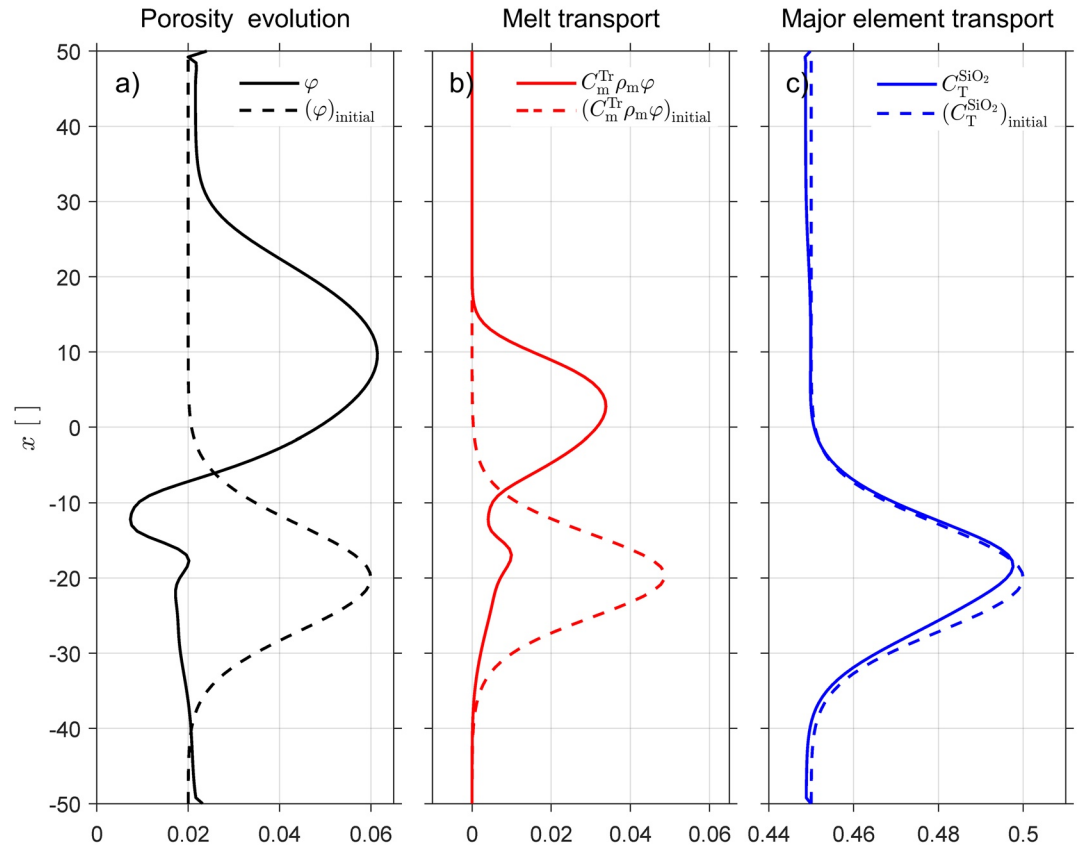
Figure 10. Comparison between porosity evolution (a), melt transport quantified by the evolution of an incompatible tracer in the melt (b; see text) and major element transport represented by transport of total silica mass fraction (c). Results of simulation S15 with conductive gradient. All variables are dimensionless. Dashed lines show the initial profiles and solid lines the profiles after 350 time steps.

tracer density, $C_m^{Tr} \rho_m \varphi$, because the maximal value of φ has moved a larger distance than the maximal value of tracer density (Figures 10a and 10b). A porosity wave propagation velocity which is slightly faster than the melt velocity agrees with results of Jordan et al. (2018) for 1D porosity waves. Nevertheless, the evolution of tracer density shows that melt is transported significantly even if the porosity wave propagates with a slightly larger velocity. The major element of Si is transported very slowly because the maximum value of $C_T^{SiO_2}$ has moved vertically only slightly (Figure 10c). Similarly, all the mass fractions, or compositions, do not vary significantly in the presented simulations and hence transport of the major elements O, Si, Mg, and Fe is minor (Figures 8 and 9). The reason for this minor variation is that the considered system is thermodynamically buffered. For example, if temperature and pressure would be constant and the system would be binary olivine then the solid MgO composition would be thermodynamically buffered and, hence, would not change even after extraction of a significant amount of iron-rich melt. Due to this thermodynamic buffering, the compositions related to the major elements of Si and Mg vary only slightly in our reactive transport model, although there is significant melt transport.

We study here the rise of an individual porosity wave causing melt migration. In nature, convection in the mantle, occurring on different spatial scales, and associated melt transport is expected to generate continued and renewed porosity and silica perturbations below the LAB. These continued perturbations can cause long-term melt migration by many subsequent porosity waves. Such long-term melt migration by subsequent porosity waves could change the compositions much more than due to an individual porosity wave, as considered here. Consequently, natural melt migration and associated chemical differentiation by reactive porosity waves should be considered as a cumulative process involving many subsequent porosity waves.

4.2. Mechanisms of Porosity Variation

The equation for the conservation of mass of MgO in the solid (see Appendix B) can be rearranged so that it describes the temporal evolution of the porosity (Appendix B):

$$\frac{1}{(1-\varphi)}\frac{d\varphi}{dt} = \frac{\partial v_s}{\partial x} + \frac{1}{\rho_s}\frac{d\rho_s}{dt} + \frac{1}{C_s^{\mathrm{MgO}}}\frac{dC_s^{\mathrm{MgO}}}{dt} - \frac{1}{C_s^{\mathrm{MgO}}\rho_s(1-\varphi)}\Gamma \tag{23}$$

where Γ is the mass transfer rate between solid and melt (Appendix B). The equation above shows that the porosity can vary in time (left-hand side of equation) due to four different mechanisms (terms on right-hand side of equation): (1) mechanical compaction or decompaction of the porous solid matrix (first term on right-hand side of Equation 23), (2) variation in density (second term), (3) variation in chemical composition (third term), and (4) mass exchange between melt and solid (fourth term). The equation above has not been used in the numerical simulations, but all terms in this equation can be post-calculated from the numerical results. We calculated the left-hand side and the right-hand side of Equation 23 from the results of simulation S15 and plotted the calculated left- and right-hand side for a specific time step (Figure 11a). The results for the left- and right-hand side are identical showing the correctness of both the derived equation and the numerical results. We also plot the four individual terms of the right-hand side of Equation 23 to determine which of the four mechanisms dominates the porosity variation (Figure 11b). For the parameters and configuration of simulation S15, mechanical compaction and decompaction is the mechanism that dominates the evolution of porosity (Figure 11b).

The effective permeability in our model depends on the porosity (Equation 15). Therefore processes such as crystallization and melting, quantified by the mass transfer rate, and the variation of densities and compositions can all affect the permeability. Hence, our model can capture many processes that affect the permeability on natural rock, such as clogging of the pore space.

4.3. Magnesium in Melt

For the applied simple chemistry, our thermodynamic model predicts an increase of the magnesium mass fraction in the melt, C_m^{MgO}, with increasing pressure with a conductive gradient (solid lines in Figures 6 and C1). Partial melting experiments of peridotite have shown also that the MgO mass fraction in the melt increases with pressure (Figure 12). The black line in Figure 12 represents the numerically modeled profile of C_m^{MgO} for a conductive thermal gradient (simulation S15). Therefore, despite the applied simplified chemistry for the mantle composition, the modeled gradient of C_m^{MgO} shows a similar trend than the experimental data. Our model shows smaller absolute values of C_m^{MgO} than the experiments, which is due to the applied simplified chemistry.

4.4. 2D Reactive Porosity Wave Model, Channelization and Melt-Rock Interaction

We present here preliminary results of a 2D model, with the aim to show that extension of the THMC model to 2D is straightforward and that melt migration in 2D models can be considerably more variable than in 1D models. A characteristic feature of porosity wave propagation in 2D and 3D is the possibility to change the shape of the propagating wave, which can be either blob-like (Figures 13a–13h) or channel-like (Figures 13i–13p; e.g., Connolly & Podladchikov, 2007; Räss et al., 2019). The shape of the propagating wave is controlled by the ratio of shear to bulk viscosity (η_s/η_v) and the ratio of decompaction to compaction bulk viscosity (η_d/η_v; e.g., Räss et al., 2019). A value of $\eta_d/\eta_v < 1$ is termed decompaction weakening. If both viscosity ratios are equal to one, the propagation is blob-like for a circular initial perturbation in porosity. If decompaction weakening is significant, then the propagating porosity wave forms a channel (e.g., Connolly & Podladchikov, 2007; Räss et al., 2019). 2D and 3D models of porosity waves are important to study the mass transport of melt because the effective mass transport predicted by 1D models is slightly less compared to predictions of 2D models (Jordan et al., 2018). The main difference compared to the 1D model is that the deformation of the viscous solid must be calculated with a 2D model for viscous flow including both shear and normal deviatoric stresses. For all other conservation equations simply the 2D advective and diffusive fluxes must be added. We present here first results of two 2D models to show the localization of flow from a blob-like (Figures 13a–13d) to a channel-like geometry (Figures 13i–13l) and associated evolutions of the total silica content (Figures 13e–13h and 13m–13p). The 2D models employ
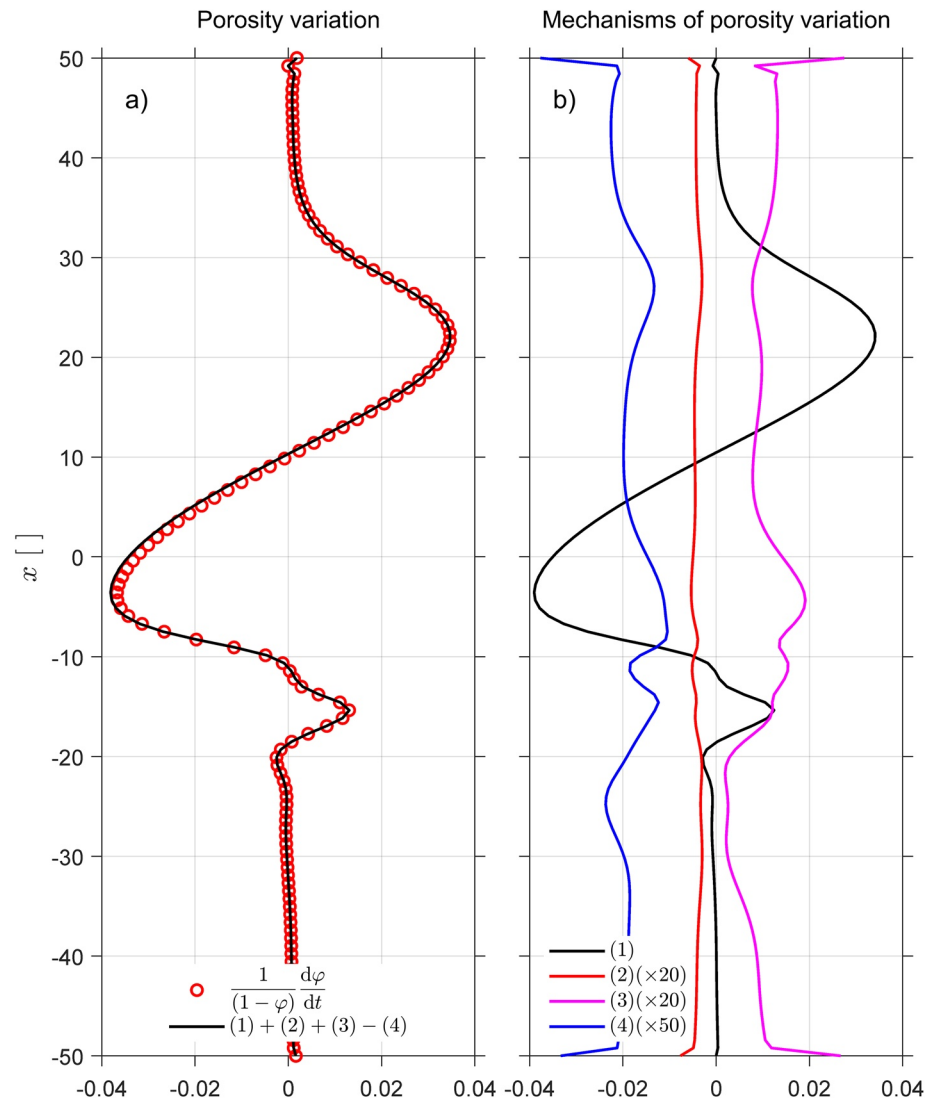
Figure 11. Quantification of four mechanisms responsible for porosity variation: (1) mechanical compaction and decompaction, (2) density variation, (3) compositional variation, and (4) solid-melt mass exchange. Panel (a) shows the vertical variation of porosity (red dots) and the black line corresponds to the combined effect of mechanisms (1), (2), (3), and (4) as specified in Equation 23. Panel (b) shows the vertical variation of the four terms quantifying the four mechanisms for porosity variation as specified in Equation 23: mechanism (1) in black, (2) red, (3) magenta, and (4) blue. The terms corresponding to mechanisms (2) to (4) have been multiplied by a factor of 20 or 50 to make their vertical variation visible compared to the vertical variation of term (1) which is significantly larger than terms (2) to (4). All results are shown for simulation S15 for a conductive gradient after 350 time steps.

mostly the same parameters as the 1D model, but, for example, the initial perturbation of the porosity has the form of a 2D Gaussian. For the model with blob-like geometry (Figures 13a–13h), we apply $\eta_s/\eta_v = 1$ and $\eta_d/\eta_v = 1$ and for the model with channel-like geometry (Figures 13i–13p) $\eta_s/\eta_v = 25$ and $\eta_d/\eta_v = 0.1$.

Panels (d), (h), (l), and (p) in Figure 13 show the chemical exchange between melt and solid in both simulations by the different evolution of the porosity and the total silica mass fraction. This exchange enables an enrichment of total silica in the solid and a differentiation of the melt in the pores.

The migration of melt by either blob-like or by channelized flow is important for understanding metasomatism in a ductile region. Following the schematic illustration of Harte et al. (1993) (Figure 14), the focusing of melt arriving in a rock to be eventually metasomatized (indicated by black arrows) has an impact on the type of metasomatism; from a pervasive metasomatism (Figure 14a), through the formation of veins (Figure 14b) to channels
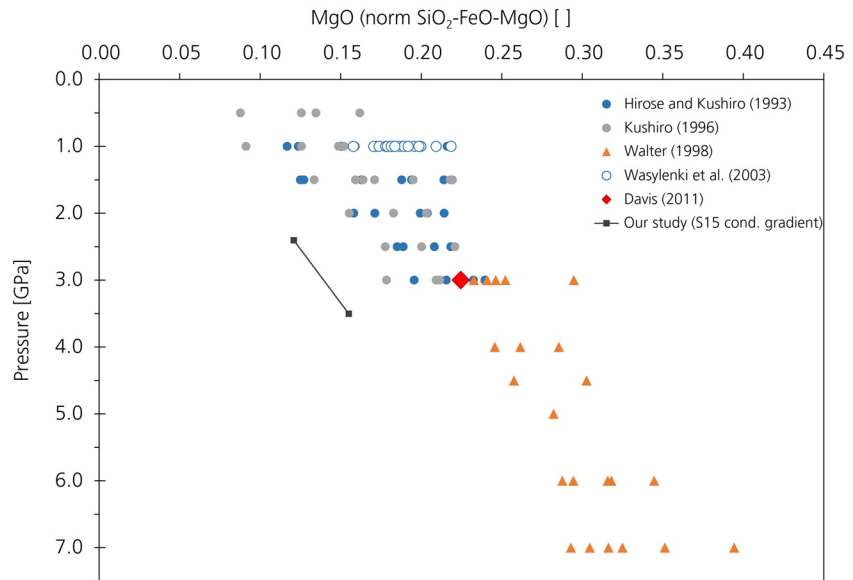
Figure 12. Magnesium melt mass fractions of five partial melting experiments of peridotite versus pressure. Filled blue circles are data from Hirose and Kushiro (1993). Filled gray circles are data from Kushiro (1996). Filled orange triangles are data from Walter (1998). Filled white circles are data from Wasylenki et al. (2003). The filled red diamond is 0% melt from Davis et al. (2011). The horizontal increase of MgO at each pressure corresponds to the increase in partial melting rate. The black line shows the overall gradient of MgO mass fraction in the melt resulting from our study without the perturbation (corresponding to the C_m^{MgO} profile in Figure 6e).

(Figure 14c). Another important aspect is the melt-rock equilibration at every time step in the model. In the 2D simulation presented in Figure 13, blob-like migration shows the importance of reaction as the chemical anomaly doesn't rise with the porosity but is accommodated by the solid via melt-rock reaction. This is illustrated by the comparison between the location of the porosity perturbation in Figure 13d and the zone with higher total SiO_2 mass fraction, which is still close to the initial perturbation indicated by the dashed circle. In contrast, in the channel-like migration the porosity is focusing and allows the chemical perturbation to rise (Figures 13l and 13p). The combination of melt-rock reaction with the type of melt migration seems therefore fundamental to understand the type of metasomatism recorded in the lithospheric mantle.

An example of melt-rock reaction has been recently considered by Tomlinson and Kamber (2021) to explain the formation and evolution of the subcontinental cratonic lithospheric mantle. Xenoliths sampled by kimberlites have revealed that the cratonic lithosphere is heterogeneous and contains olivine with high magnesium content (Fo92−94), which requires extensive melting (Boyd & Mertzman, 1987; Herzberg, 1993). One interesting feature of this peridotitite xenolith suite is the lower MgO/SiO_2 ratio for a given magnesium number (Mg#) of Archean subcontinental cratonic lithosphere relative to younger subcontinental lithospheric mantle. While various hypotheses have been proposed to explain this feature (e.g., Boyd & Mertzman, 1987; Herzberg, 1993), Tomlinson and Kamber (2021) suggest that silica enrichment in cratonic lithosphere could be associated to the migration of komatiite magma produced in episodic hot asthenospheric upwellings, which interact with previously depleted peridotite. Their melt-peridotite interaction is supported by THERMOCALC calculations, but no physical aspect on melt migration is considered. Although our thermodynamic calculation does not yet allow to predict natural melt-peridot chemical interactions due to our simplified chemical system, which does not consider pyroxene crystallization or dissolution, the mechanical aspects of our model show the importance of decompaction weakening and provide some new insights of melt-percolation within the ductile mantle, supporting potential channelization of melt passing through a cratonic lithosphere.

4.5. Estimates of Melt Velocity

We can use the characteristic values of L_c and t_c to calculate a dimensional melt velocity from the numerically calculated melt velocity, by applying representative values for melt viscosity, bulk viscosity and porosity. Using a
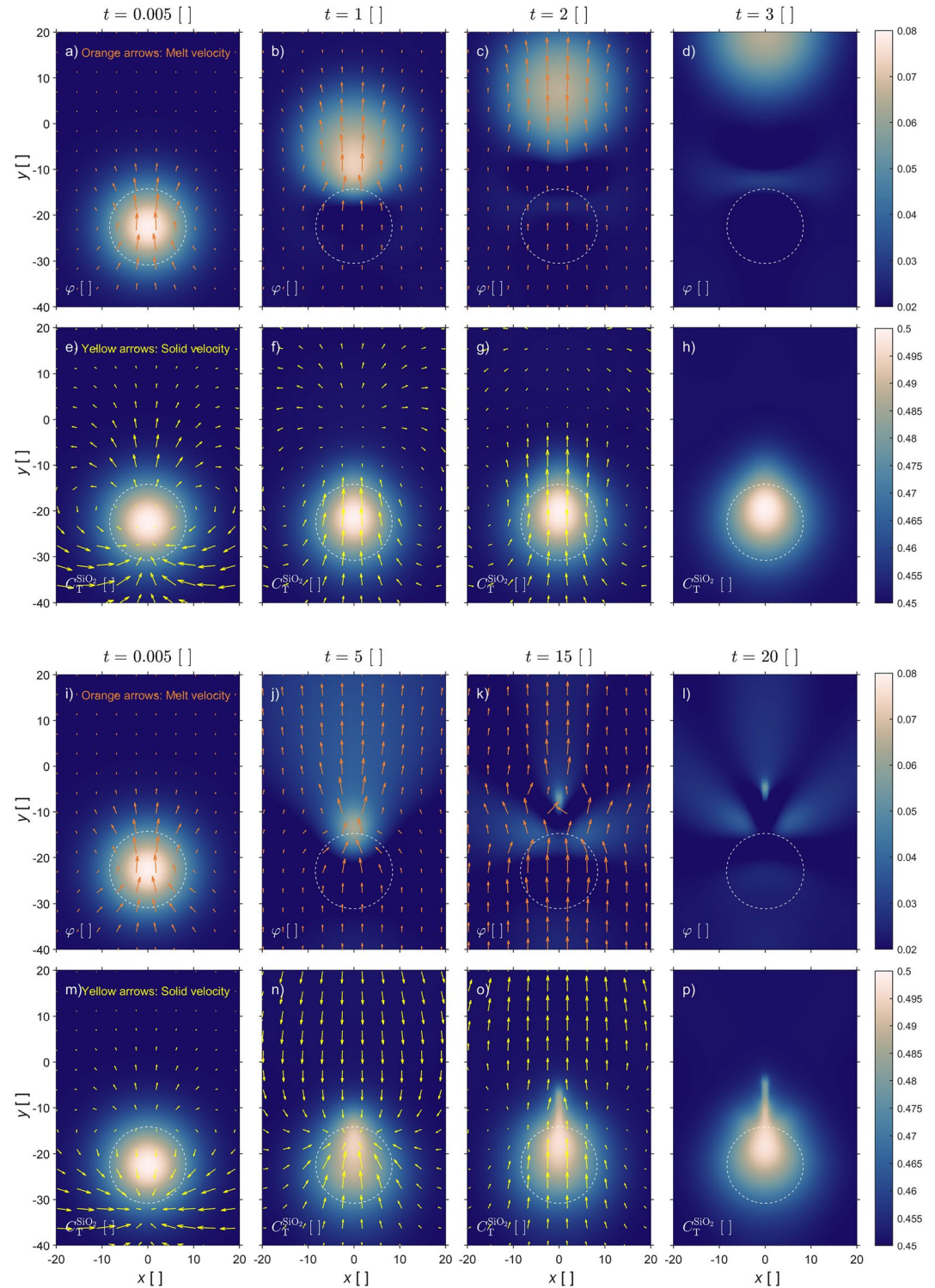
Figure 13. Time evolution of two 2D melt migration models by reactive porosity waves. Panels (a–d) show the porosity and panels (e–h) the total silica mass fraction for the blob-like simulation at four different dimensionless times (0.005, 1, 2, and 3). $(\eta_s/\eta_v) = 1$ and $(\eta_d/\eta_v) = 1$ for the blob-like simulation. Panels (i–l) show the porosity and panels (m–p) the total silica mass fraction for the channel-like simulation at four different dimensionless times (0.005, 5, 15, and 20). $(\eta_s/\eta_v) = 25$ and $(\eta_d/\eta_v) = \eta_v/100 = 0.1$ for the channel-like simulation. Orange arrows show melt velocity, yellow arrows show solid velocity, and dashed circles the position of initial perturbations. All variables are dimensionless.

Modal metasomatism: various degrees of channelizing of the melt flow
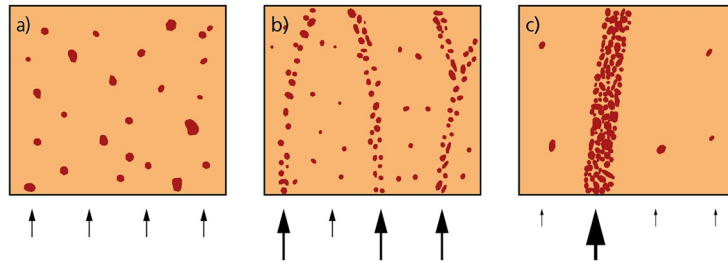
Figure 14. Schematic illustration showing the various degrees of channelizing of the melt flow as function of the distribution of melt flux (see text). Panel (a) shows pervasive metasomatism, panel (b) shows metasomatism by formation of veins and panel (c) by formation of a channel. Redrawn form Harte et al. (1993).

porosity φ of 2%, the effective permeability is in the order of $k = 10^{-7} \cdot \varphi^3 = 8 \cdot 10^{-13}$ (m²) (e.g., Connolly & Podladchikov, 2007). We assume values for melt viscosity η_m between 0.1 and 10 (Pa·s) (e.g., McKenzie, 1989). We further assume that the bulk viscosity η_v is identical to the shear viscosity around the LAB and use 10^{19} (Pa·s), in agreement with numerical lithosphere subduction simulations of Bessat et al. (2020) (Figure 2). The applied melt density is the reference density ($\rho_{m,0} = 3,863$ (kg m⁻³)). Taking a typical velocity of 12 from the two simulations S15 (red dots in the top middle in Figures 7a and 7b), we obtain a dimensional melt velocity between 1 and 115 (m·yr⁻¹). Modifying the porosity φ to 1% and 0.5%, and the associated permeability, and using a melt viscosity η_m of 0.1 (Pa·s), which seems more realistic for low degree melts rising in the lithosphere, we obtain velocities between 14.3 (m·yr⁻¹) and 1.8 (m·yr⁻¹) for a porosity of 1% and 0.5%, respectively. Using a larger melt viscosity η_m of 10 (Pa·s), as used by Connolly et al. (2009) to estimate melt velocity at mid ocean ridges, we obtain 14 and 1.8 (cm·yr⁻¹), respectively. The melt velocities estimated above agree to first order with melt transport velocities deduced from centrifuge experiments by Connolly et al. (2009), which are 2–150 (m·yr⁻¹) and considered applicable for melt rising at mid-ocean-ridges.

5. Conclusions

We present a new numerical model for melt migration by porosity waves in a viscous solid coupled to chemical differentiation. The model is based on the coupling of a THMC transport model with thermodynamic results that have been precomputed by Gibbs energy minimization. For the considered system of forsterite-fayalite-silica, the solid and melt densities and the mass fractions of MgO and SiO_2 in both solid and melt are fully mobile, and all densities and mass fractions vary with P, T, and $C_T^{SiO_2}$. Therefore, the model is suitable to investigate chemical differentiation, metasomatism, clogging and melt-rock interaction during melt migration.

The thermodynamic results show that the sensitivity of solid and melt densities to variations in P, T, and $C_T^{SiO_2}$, considered in the THMC model via coefficients α, β, and γ, respectively, can be considerably different. The same applies for the solid and melt mass fractions of MgO and SiO_2. Particularly, the sensitivity to variations in $C_T^{SiO_2}$ is considerably different for the densities and MgO and SiO_2 mass fractions. Hence, it is important to consider these different dependencies of densities and mass fractions on variations in P, T, and $C_T^{SiO_2}$ in a THMC melt migration model and to determine these dependencies with thermodynamic calculations.

The developed THMC transport model can generate porosity waves. The initial variation of porosity and total silica concentration has a strong impact on the melt velocity. For minor initial porosity variations of half a percent (0.005), variations in total silica content cause variations in solid and melt densities and trigger porosity waves. Hence, variations in chemistry can trigger melt migration by porosity waves in regions with minor porosity variation. Also, the employed thermal gradient in the model, either adiabatic or conductive, has an impact on the melt velocity, with higher velocities resulting from an adiabatic gradient. For conditions applicable to the LAB, the densities for an adiabatic gradient increase with depth, while for a conductive gradient the densities decrease with depth. The thermal gradient, therefore, has a considerable impact on the vertical variation of solid and melt densities and mass fractions and, hence, on the chemical differentiation during melt migration. Application of a range of typical lithosphere values for porosity, permeability, melt and compaction viscosities provides reasonable melt velocities between 10 (cm·yr⁻¹) and 100 (m·yr⁻¹).

Our results show that the porosity variation is controlled by four mechanisms: (a) mechanical compaction and decompaction of the porous solid matrix, (b) density variations, (c) compositional variations, and (d) mass exchange between solid and melt. In the presented simulations, mechanical (de)compaction is the dominant process for porosity variation.

Using incompatible tracers, we show that significant melt and mass is transported by porosity waves, although the porosity wave propagates with a velocity slightly larger than the melt velocity; a result in agreement with previous studies. In contrast, the transport of the major elements Mg and Si is minor since these elements are thermodynamically buffered.

The preliminary 2D version of the THMC model can generate blob-like and channel-like porosity waves. First 2D results show that the total silica mass transport is more efficient by channel-like porosity waves than by blob-like porosity waves, which has important implications for understanding metasomatism during melt migration across the ductile lithosphere.

Appendix A: THMC Model Equations

A general conservation equation without a source term in 1D for any variable, here named B (per unit volume), has the form:

$$\frac{\partial B}{\partial t} = -\frac{\partial}{\partial x} q_A - \frac{\partial}{\partial x} q_D \tag{A1}$$

where t is the time, q_A is the advective flux, and q_D is the diffusive flux.

A porous medium, with porosity φ, is composed of a solid skeleton (solid phase) with density ρ_s and a melt phase in the pores with density ρ_m. The total mass of the medium, having total density ρ_T, is the sum of the mass of melt in pores and the mass of the solid:

$$B = \rho_m \varphi + \rho_s (1 - \varphi) = \rho_T \tag{A2}$$

The advective flux for the total mass is:

$$q_A = \rho_m \varphi v_m + \rho_s (1 - \varphi) v_s \tag{A3}$$

where v_m and v_s are the melt and solid velocities, respectively. There is no diffusive flux in the conservation of the total mass, hence:

$$q_D = 0 \tag{A4}$$

Therefore, the conservation equation for total mass is:

$$\frac{\partial}{\partial t} (\rho_m \varphi + \rho_s (1 - \varphi)) = -\frac{\partial}{\partial x} (\rho_m \varphi v_m + \rho_s (1 - \varphi) v_s) \tag{A5}$$

The force balance for the melt follows Darcy's law:

$$\varphi (v_m - v_s) = -\frac{k\varphi^3}{\eta_m} \left(\frac{\partial P_m}{\partial x} + \rho_m g \right) \tag{A6}$$

where k is the permeability, η_m is the melt viscosity, P_m is the melt pressure, and g is the gravitational acceleration. To introduce the Darcy's force balance in the total mass conservation equation, it is useful to modify Equation A6 by subtracting and adding v_s to v_m:

$$\frac{\partial}{\partial t} (\rho_m \varphi + \rho_s (1 - \varphi)) = -\frac{\partial}{\partial x} (\rho_m \varphi (v_m - v_s + v_s) + \rho_s (1 - \varphi) v_s) \tag{A7}$$

Equation A8 can be rewritten as:

$$\frac{\partial}{\partial t} (\rho_m \varphi + \rho_s (1 - \varphi)) = -\frac{\partial}{\partial x} \left(-\rho_m \frac{k\varphi^3}{\eta_m} \left(\frac{\partial P_m}{\partial x} + \rho_m g \right) + \rho_m \varphi v_s + \rho_s (1 - \varphi) v_s \right) \tag{A8}$$

Equation A9 can be simplified by collecting terms in front of v_s:

$$\frac{\partial}{\partial t}\left(\rho_m \varphi + \rho_s (1-\varphi)\right) = -\frac{\partial}{\partial x}\left(-\rho_m \frac{k\varphi^3}{\eta_m}\left(\frac{\partial P_m}{\partial x} + \rho_m g\right) + \rho_T v_s\right) \tag{A9}$$

The total mass of magnesium (MgO) considers the concentration of MgO in the melt and in the solid:

$$B = C_m^{MgO} \rho_m \varphi + C_s^{MgO} \rho_s (1-\varphi) = M_T^{MgO} \tag{A10}$$

where C_m^{MgO} and C_s^{MgO} are, respectively, the mass fractions (C_m^{MgO} = mass of MgO in the melt/total mass of melt; C_s^{MgO} = mass of MgO in the solid/total mass of solid) of MgO in the melt and in the solid. The advective flux for the total mass of MgO is:

$$q_A = C_m^{MgO} \rho_m \varphi v_m + C_s^{MgO} \rho_s (1-\varphi) v_s \tag{A11}$$

Assuming an ideal solution, the diffusive flux is described by Fick's law that describes the molecular diffusion of MgO in the melt and in the solid:

$$q_D = -D_m^{MgO} \rho_m \varphi \frac{\partial C_m^{MgO}}{\partial x} - D_s^{MgO} \rho_s (1-\varphi) \frac{\partial C_s^{MgO}}{\partial x} \tag{A12}$$

where D_m^{MgO} and D_s^{MgO} are the effective diffusivities of MgO in the melt and in the solid (e.g., Nauman & He, 2001). Therefore, the conservation equation for total mass of MgO is:

$$\frac{\partial}{\partial t}\left(C_m^{MgO} \rho_m \varphi + C_s^{MgO} \rho_s (1-\varphi)\right) = -\frac{\partial}{\partial x}\left(C_m^{MgO} \rho_m \varphi v_m + C_s^{MgO} \rho_s (1-\varphi) v_s - D_m^{MgO} \rho_m \varphi \frac{\partial C_m^{MgO}}{\partial x}\right.$$
$$\left. - D_s^{MgO} \rho_s (1-\varphi) \frac{\partial C_s^{MgO}}{\partial x}\right) \tag{A13}$$

The total mass per unit of volume SiO_2 considers the concentration of SiO_2 in the melt and in the solid:

$$B = C_m^{SiO_2} \rho_m \varphi + C_s^{SiO_2} \rho_s (1-\varphi) = M_T^{SiO_2} \tag{A14}$$

where $C_m^{SiO_2}$ and $C_s^{SiO_2}$ are respectively the mass fractions ($C_m^{SiO_2}$ = mass of SiO_2 in the melt/total mass of melt; $C_s^{SiO_2}$ = mass of SiO_2 in the solid/total mass of solid) of SiO_2 in the melt and in the solid. The advective flux for the total mass of SiO_2 is:

$$q_A = C_m^{SiO_2} \rho_m \varphi v_m + C_s^{SiO_2} \rho_s (1-\varphi) v_s \tag{A15}$$

For an ideal solution, the diffusive flux is described by Fick's law that describes the molecular diffusion of SiO_2 in the melt and in the solid:

$$q_D = -D_m^{SiO_2} \rho_m \varphi \frac{\partial C_m^{SiO_2}}{\partial x} - D_s^{SiO_2} \rho_s (1-\varphi) \frac{\partial C_s^{SiO_2}}{\partial x} \tag{A16}$$

where $D_m^{SiO_2}$ and $D_s^{SiO_2}$ are the effective diffusivities of SiO_2 in the melt and in the solid (e.g., Nauman & He, 2001). Therefore, conservation equation for total mass of SiO_2 is:

$$\frac{\partial}{\partial t}\left(C_m^{SiO_2} \rho_m \varphi + C_s^{SiO_2} \rho_s (1-\varphi)\right) = -\frac{\partial}{\partial x}\left(C_m^{SiO_2} \rho_m \varphi v_m + C_s^{SiO_2} \rho_s (1-\varphi) v_s - D_m^{SiO_2} \rho_m \varphi \frac{\partial C_m^{SiO_2}}{\partial x}\right.$$
$$\left. - D_s^{SiO_2} \rho_s (1-\varphi) \frac{\partial C_s^{SiO_2}}{\partial x}\right) \tag{A17}$$

The total thermal energy of the medium is:

$$U_m(P,T) = \int_{T_{ref}}^{T} \left(c_{p_m}(P,T') \rho_m(P,T') \right) dT'$$

$$U_s(P,T) = \int_{T_{ref}}^{T} \left(c_{p_s}(P,T') \rho_s(P,T') \right) dT' \tag{A18}$$

$$B = U_m \varphi + U_s(1-\varphi) = U_T$$

where C_{p_m} and C_{p_s} are specific heat capacity of the melt and the solid and T is the temperature. The advective flux for thermal energy is:

$$q_A = U_m \varphi v_m + U_s(1-\varphi) v_s \tag{A19}$$

Assuming that the temperature in the solid and fluid is identical, the diffusive flux is described by Fourier'law:

$$q_D = -\lambda_T \frac{\partial T}{\partial x} \tag{A20}$$

where $\lambda_T = (\lambda_m \varphi + \lambda_s(1-\varphi))$ and λ_m and λ_s are the thermal conductivity of melt and solid, respectively. The conservation equation for the energy takes the form of:

$$\frac{\partial}{\partial t}(U_m \varphi + U_s(1-\varphi)) = -\frac{\partial}{\partial x}\left(U_m \varphi v_m + U_s(1-\varphi)v_s - \lambda_T \frac{\partial T}{\partial x}\right) \tag{A21}$$

The other mechanical equations that close the system of equations are presented in Section 2.2, Equations 13, 14, 16 and 17.

Appendix B: Equation for Porosity Evolution

In our approach, we use the equation for the conservation of total mass and do not use two separate equations for the conservation of solid and melt mass. The same applies for the mass conservation equations for MgO and SiO_2. However, to investigate the different mechanisms which control the variation of porosity, it is useful to consider the mass conservation equations for solid and melt separately. Following the approach of McKenzie (1984), the conservation of mass (per unit volume) of MgO in the melt and in the solid can be written as

$$\frac{\partial\left(C_m^{MgO}\rho_m\varphi\right)}{\partial t} + \frac{\partial}{\partial x}\left(C_m^{MgO}\rho_m\varphi v_m\right) = -\Gamma \tag{B1}$$

$$\frac{\partial\left(C_s^{MgO}\rho_s(1-\varphi)\right)}{\partial t} + \frac{\partial}{\partial x}\left(C_s^{MgO}\rho_s(1-\varphi)v_s\right) = \Gamma \tag{B2}$$

where Γ is the mass transfer rate. This mass transfer rate can be post-calculated from the numerical results, because the spatial and temporal evolution of concentrations, densities, porosity and velocities are calculated during the simulations. Summing the two equations above provides the equation of conservation of total mass of MgO, in which Γ is eliminated, as used in our numerical model. The equation for the conservation of mass of MgO in the solid can be reformulated into an equation describing the temporal variation of the porosity. First, the spatial derivative term is separated into two terms (by using the product rule) to (a) bring the solid velocity in front of the spatial derivative and (b) generate a term with the divergence of the solid velocity:

$$\frac{\partial\left(C_s^{MgO}\rho_s(1-\varphi)\right)}{\partial t} + v_s\frac{\partial}{\partial x}\left(C_s^{MgO}\rho_s(1-\varphi)\right) + C_s^{MgO}\rho_s(1-\varphi)\frac{\partial v_s}{\partial x} = \Gamma \tag{B3}$$

The two left-most terms of the equation above are now combined to the material time derivative, d/dt (including the advection term), of the mass of MgO in the solid

$$\frac{d\left(C_s^{MgO}\rho_s(1-\varphi)\right)}{dt} + C_s^{MgO}\rho_s(1-\varphi)\frac{\partial v_s}{\partial x} = \Gamma \tag{B4}$$

Next, the time derivative can be separated into three terms (using again the product rule)

$$C_s^{MgO} \rho_s \frac{d(1-\varphi)}{dt} + C_s^{MgO}(1-\varphi)\frac{d\rho_s}{dt} + \rho_s(1-\varphi)\frac{dC_s^{MgO}}{dt} + C_s^{MgO}\rho_s(1-\varphi)\frac{\partial v_s}{\partial x} = \Gamma \tag{B5}$$

Finally, the equation above is rearranged so that the time derivative of the porosity is on the left-hand side of the equation and all other terms are on the right-hand side:

$$\frac{1}{(1-\varphi)}\frac{d\varphi}{dt} = \frac{\partial v_s}{\partial x} + \frac{1}{\rho_s}\frac{d\rho_s}{dt} + \frac{1}{C_s^{MgO}}\frac{dC_s^{MgO}}{dt} - \frac{1}{C_s^{MgO}\rho_s(1-\varphi)}\Gamma \tag{B6}$$

The equation above shows that the porosity can vary in time due to four different mechanisms, expressed by the four terms on the right-hand side of the equation: (a) mechanical compaction or decompaction of the porous solid matrix (divergence of solid velocity), (b) temporal variation in density, (c) temporal variation in concentration (or composition), and (d) mass exchange between melt and solid. All four mechanisms are considered in our model.

Appendix C: Additional Figures and Tables

In this appendix, we show additional results with four figures and a table including the numerical pseudo-transient time steps used in the THMC code.
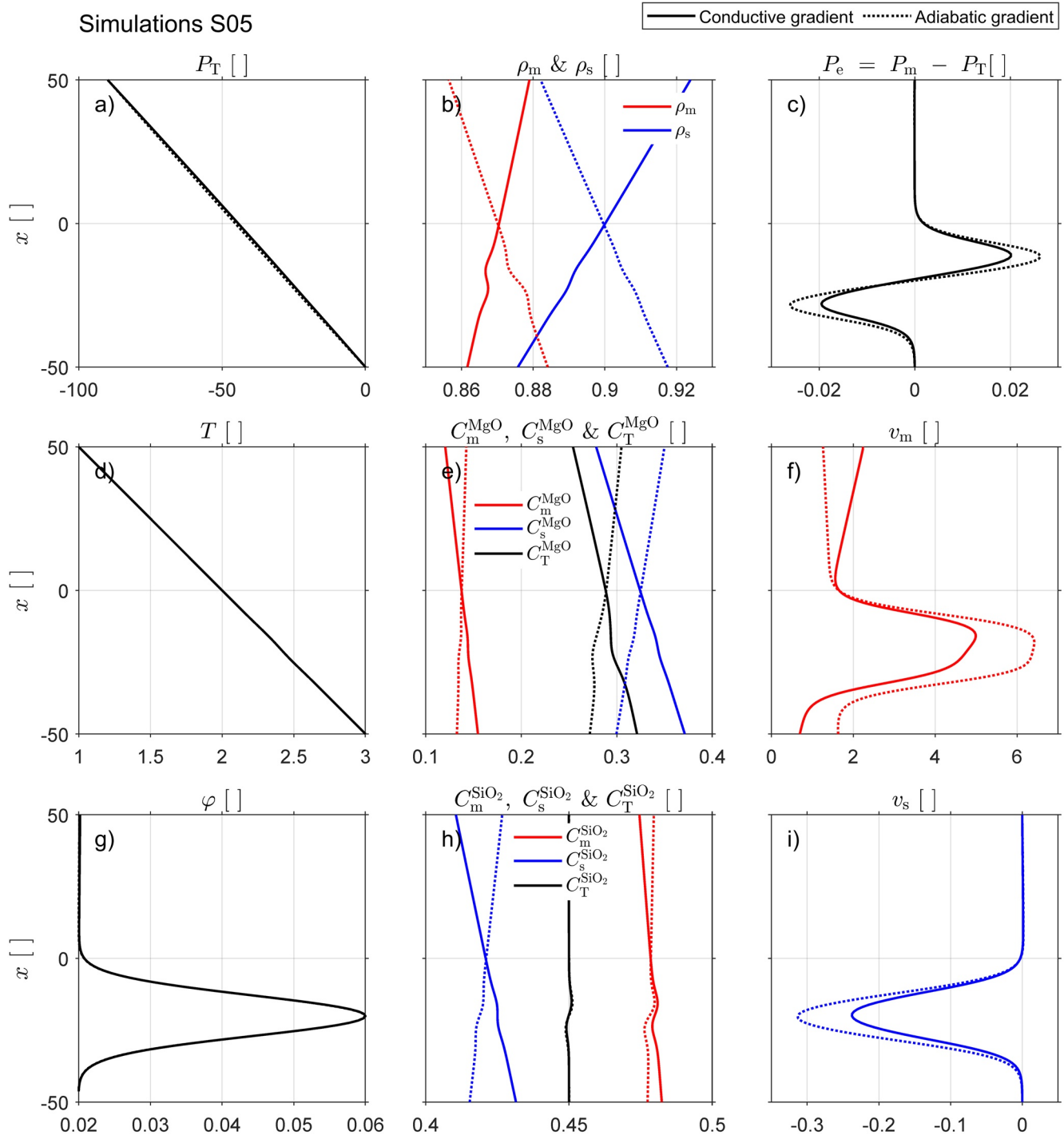
Figure C1. Initial profiles for simulation S05 for a conductive gradient (solid lines) and for an adiabatic gradient (dashed lines). All variables are dimensionless. Panel (a) shows total pressure. Panel (b) shows melt density (red lines) and solid density (blue lines). Panel (c) shows effective pressure, positive values indicate decompaction while negative values indicate compaction. Panel (d) shows temperature. Panel (e) shows magnesium mass fraction in melt (red lines) and in solid (blue lines) and total magnesium mass fraction (black lines). Panel (f) shows melt velocity. Panel (g) shows porosity. Panel (h) shows silica mass fraction in melt (red lines) and in the solid (blue lines) and total silica mass fraction (black lines). Panel (i) shows solid velocity.
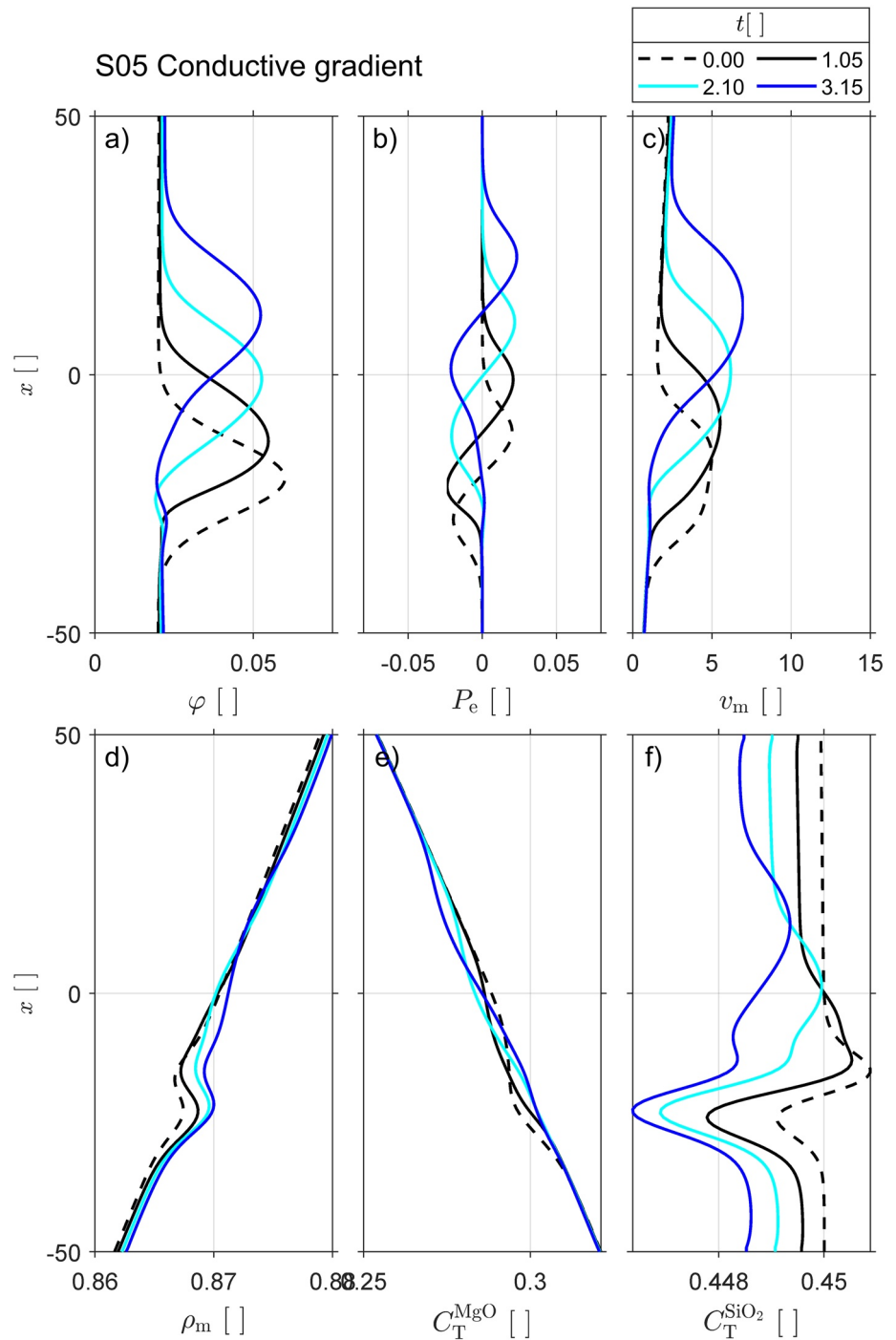
Figure C2. Time evolution of six variables for simulation S05 with conductive gradient, all variables are dimensionless. Panel (a) shows porosity, panel (b) shows effective pressure, panel (c) shows melt velocity, panel (d) shows melt density, panel (e) shows total magnesium mass fraction, and panel (f) shows total silica mass fraction. Four time steps are chosen at different dimensional times: $t = 0$ with dashed line (corresponding to the initial profiles, solid lines, in Figure C1 for each variable), $t = 1.05$ with black line, $t = 2.10$ with light blue, and $t = 3.15$ with dark blue (see legend).
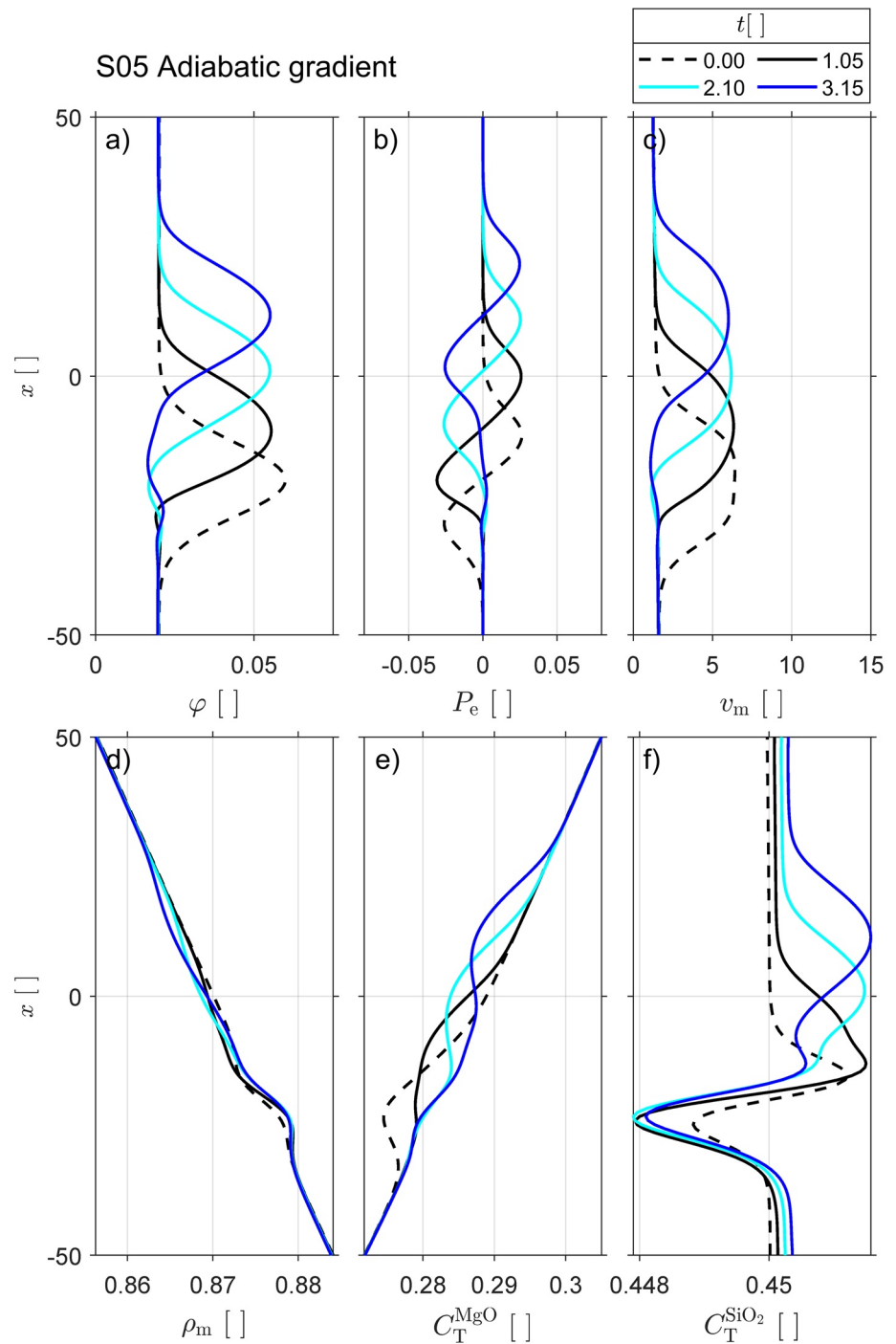
Figure C3. Time evolution of six variables for simulation S05 with adiabatic gradient, all variables are dimensionless Panel (a) shows porosity, panel (b) shows effective pressure, panel (c) shows melt velocity, panel (d) shows melt density, panel (e) shows total magnesium mass fraction, and panel (f) shows total silica mass fraction. Four time steps are chosen at different dimensional times: $t = 0$ with dashed line (corresponding to the initial profiles, dashed lines, in Figure C1 for each variable), $t = 1.05$ with black line, $t = 2.10$ with light blue, and $t = 3.15$ with dark blue (see legend).
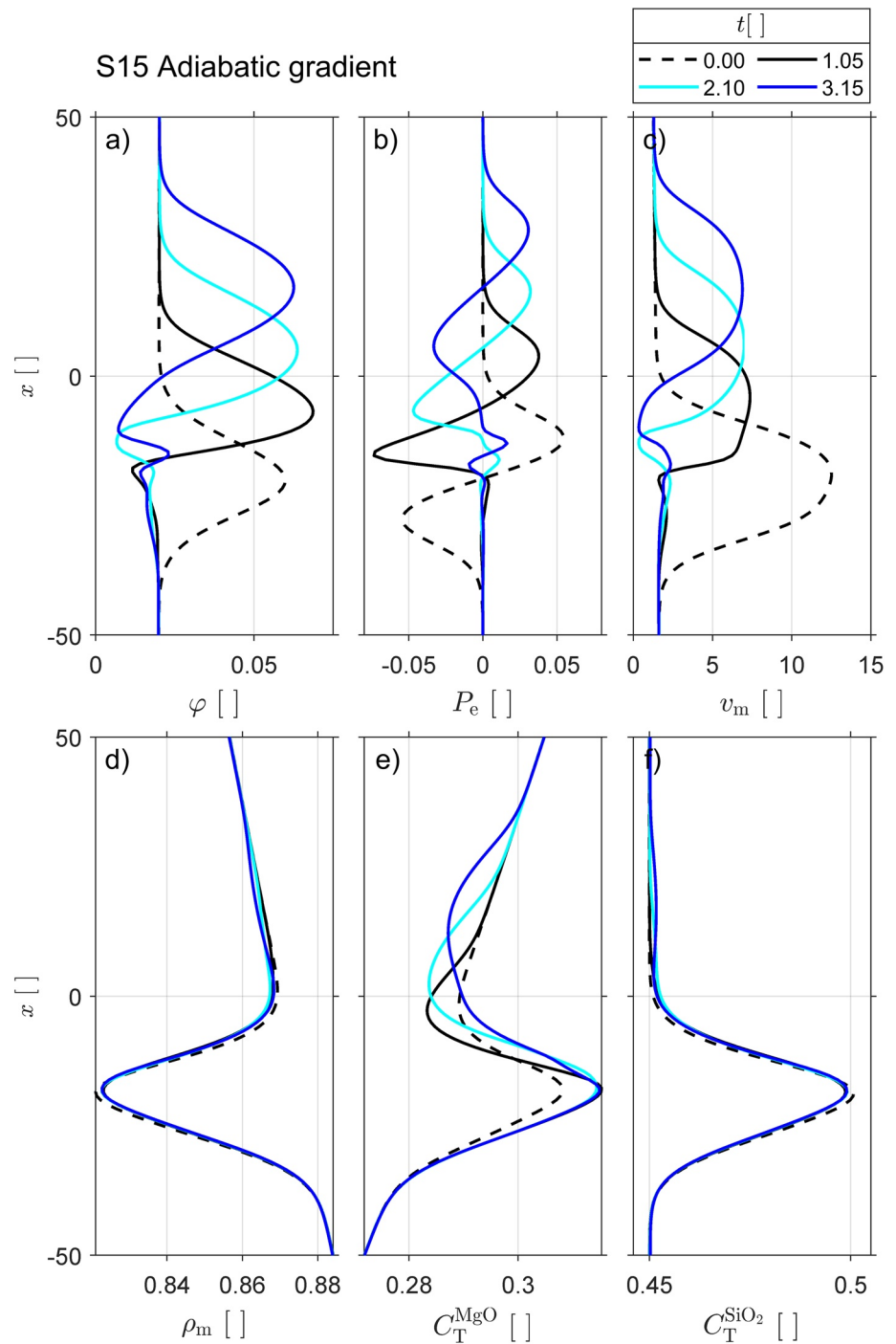
Figure C4. Time evolution of six variables for simulation S15 with adiabatic gradient, all variables are dimensionless. Panel (a) shows porosity, panel (b) shows effective pressure, panel (c) shows melt velocity, panel (d) shows melt density, panel (e) shows total magnesium mass fraction, and panel (f) shows total silica mass fraction. Four time steps are chosen at different dimensional times: $t = 0$ with dashed line (corresponding to the initial profiles, dashed lines, in Figure 6 for each variable), $t = 1.05$ with black line, $t = 2.10$ with light blue, and $t = 3.15$ with dark blue (see legend).

Table C1
Numerical Pseudo-Transient Time Step Used in the THMC Simulations

Pseudo-transient time step	
For the melt pressure	$\Delta t_P{}^{TP} = \frac{1}{8} \frac{dx^2}{max\left(k/\eta_m\right) \cdot \left(\varphi/\varphi_0\right)^3}$
For the porosity	$\Delta t_\varphi{}^{TP} = dt$
For the total silica content	$\Delta t_{C_T^{SiO_2}}{}^{TP} = dt$
For the temperature	$\Delta t_T{}^{TP} = \frac{1}{40 \rho_T c_{p_T}} \frac{dx^2}{max\left(\lambda_m/\rho_T c_{p_T}\right)}$
For the solid velocity	$\Delta t_{v_s}{}^{TP} = \frac{1}{6} \frac{dx^2}{\eta_s}$

Note. THMC, thermo-hydro-mechanical-chemical.

Appendix D: Thermodynamic Calculations

D1. Transformation From Molar Fractions Into Mass Fractions

To use molar concentrations in the mass conservation equations of the thermo-hydro-mechanical-chemical (THMC) transport model, we first transform these concentrations into olivine phase mass fractions:

$$C_m^{foL} = \frac{C_{m,[mol]}^{foL} \cdot m_m^{foL}}{\left(C_{m,[mol]}^{foL} \cdot m_m^{foL}\right) + \left(C_{m,[mol]}^{faL} \cdot m_m^{faL}\right)} \tag{D1a}$$

$$C_m^{faL} = \frac{C_{m,[mol]}^{faL} \cdot m_m^{faL}}{\left(C_{m,[mol]}^{foL} \cdot m_m^{foL}\right) + \left(C_{m,[mol]}^{faL} \cdot m_m^{faL}\right)} \tag{D1b}$$

$$C_s^{fo} = \frac{C_{s,[mol]}^{fo} \cdot m_s^{fo}}{\left(C_{s,[mol]}^{fo} \cdot m_s^{fo}\right) + \left(C_{s,[mol]}^{fa} \cdot m_s^{fa}\right)} \tag{D1c}$$

$$C_s^{fa} = \frac{C_{s,[mol]}^{fa} \cdot m_s^{fa}}{\left(C_{s,[mol]}^{fo} \cdot m_s^{fo}\right) + \left(C_{s,[mol]}^{fa} \cdot m_s^{fa}\right)} \tag{D1d}$$

where $m_m^{foL}, m_m^{faL}, m_m^{fo}$ and m_m^{fa} are, respectively, the molar mass of forsterite and fayalite liquid for the melt part and forsterite and fayalite for the solid part. We transform these olivine phase mass fractions into oxide mass fractions of MgO, FeO, and SiO_2:

$$C_{m,i}^{MgO} = C_m^{foL} \cdot M_r^{MgO} \cdot nb^{MgO} \tag{D2a}$$

$$C_{m,i}^{FeO} = \left(1 - C_m^{foL}\right) \cdot M_r^{FeO} \cdot nb^{FeO} \tag{D2b}$$

$$C_{m,i}^{SiO_2} = \left(C_m^{foL} + 1 - C_m^{foL}\right) \cdot M_r^{SiO_2} \cdot nb^{SiO_2} \tag{D2c}$$

where M_r^{MgO}, M_r^{FeO}, and $M_r^{SiO_2}$ are molecular weight (i.e., relative molecular mass) of oxides ($M_r^{MgO} = 0.0403$ (kg·mol^{-1}), $M_r^{FeO} = 0.0708$ (kg·mol^{-1}), and $M_r^{SiO_2} = 0.0601$ (kg·mol^{-1})), nb^{MgO}, nb^{FeO}, and nb^{SiO_2} correspond to the number of times each oxide is in the olivine formula ($nb^{MgO} = nb^{FeO} = 2$ and $nb^{SiO_2} = 1$), subscript i indicates that the oxide mass fractions $C_{m,i}^{MgO}$, $C_{m,i}^{FeO}$, and $C_{m,i}^{SiO_2}$ are not normalized. For the normalization, each oxide mass fraction is divided by the sum of these three oxide mass fractions:

$$C_m^{MgO} = \frac{C_{m,i}^{MgO}}{C_{m,i}^{MgO} + C_{m,i}^{FeO} + C_{m,i}^{SiO_2}} \tag{D3a}$$

$$C_m^{FeO} = \frac{C_{m,i}^{FeO}}{C_{m,i}^{MgO} + C_{m,i}^{FeO} + C_{m,i}^{SiO_2}} \tag{D3b}$$

$$C_m^{SiO_2} = \frac{C_{m,i}^{SiO_2}}{C_{m,i}^{MgO} + C_{m,i}^{FeO} + C_{m,i}^{SiO_2}} \tag{D3c}$$

C_m^{MgO}, C_m^{FeO}, and $C_m^{SiO_2}$ are the oxide mass fractions that we use in the THMC model. We proceed with the same approach to calculate the values for the solid part, C_s^{MgO}, C_s^{FeO}, and $C_s^{SiO_2}$.

D2. Calculation of γ

We calculate the γ for $C_m^{SiO_2}$ and $C_s^{SiO_2}$ as follow:

$$\gamma_{C_m^{SiO_2}} = \left(\frac{C_{m,exp}^{SiO_2} - C_{m,0}^{SiO_2}}{C_{T,exp}^{SiO_2} - C_{T,0}^{SiO_2}} \right) \Bigg/ C_{m,0}^{SiO_2} \tag{D4a}$$

$$\gamma_{C_s^{SiO_2}} = \left(\frac{C_{s,exp}^{SiO_2} - C_{s,0}^{SiO_2}}{C_{T,exp}^{SiO_2} - C_{T,0}^{SiO_2}} \right) \Bigg/ C_{s,0}^{SiO_2} \tag{D4b}$$

For the density calculation, we use the thermodynamic data of Holland and Powell (1998) and the different minerals and liquids Mg-Fe endmembers are recalculated from experimental data of Davis et al. (2011). In these calculations, we use the following endmembers: for the solid part, forsterite (fo; Mg_2SiO_4) and fayalite (fa; Fe_2SiO_4) for olivine; enstatite (en; $Mg_2Si_2O_6$) and ferrosilite (fs; $Fe_2Si_2O_6$) for orthopyroxene; diopside (di; $CaMgSi_2O_6$) and hedenbergite (hed; $CaFeSi_2O_6$) for clinopyroxene; pyrope (py; $Mg_3Al_2Si_3O_{12}$) and almandine (alm; $Fe_3Al_2Si_3O_{12}$) for garnet. We consider also quartz (q; SiO_2). For the melt part, we consider forsterite liquid (foL), fayalite liquid (faL), and quartz liquid (qL). The abbreviations in brackets correspond to the nomenclature of Holland and Powell (1998).

Data Availability Statement

All numerical results have been generated with a self-developed MATLAB code, which is available on the platform Zenodo under https://doi.org/10.5281/zenodo.5777554.

References

Aharonov, E., Spiegelman, M., & Kelemen, P. B. (1997). Three-dimensional flow and reaction in porous media: Implications for the Earth's mantle and sedimentary basins. *Journal of Geophysical Research*, *102*(B7), 14821–14833. https://doi.org/10.1029/97jb00996

Aharonov, E., Whitehead, J. A., & Kelemen, P. B. (1995). Channeling instability of upwelling melt in the mantle. *Journal of Geophysical Research*, *100*(B10), 20433–20450. https://doi.org/10.1029/95jb01307

Ahern, J., & Turcotte, D. (1979). Magma migration beneath an ocean ridge. *Earth and Planetary Science Letters*, *45*(1), 115–122. https://doi.org/10.1016/0012-821x(79)90113-4

Beinlich, A. J. T., Vrijmoed, J. C., Tominaga, M. M. T., & Podladchikov, Y. Y. (2020). Instantaneous rock transformations in the deep crust driven by reactive fluid flow. *Nature Geoscience*, *13*(4), 307–311. https://doi.org/10.1038/s41561-020-0554-9

Bessat, A., Duretz, T., Hetényi, G., Pilet, S., & Schmalholz, S. M. (2020). Stress and deformation mechanisms at a subduction zone: Insights from 2-d thermomechanical numerical modelling. *Geophysical Journal International*, *221*(3), 1605–1625. https://doi.org/10.1093/gji/ggaa092

Best, M. (1974). Mantle-derived amphibole within inclusions in alkalic-basaltic lavas. *Journal of Geophysical Research*, *79*(14), 2107–2113. https://doi.org/10.1029/jb079i014p02107

Boyd, F., & Mertzman, S. (1987). Composition and structure of the Kaapvaal lithosphere, Southern Africa. In B. O. Mysen (Ed.) *Magmatic Processes: Physicochemical Principles, The Geochemical Society* (Vol. 1, pp. 13–24).

Burov, E. B. (2011). Rheology and strength of the lithosphere. *Marine and Petroleum Geology*, *28*(8), 1402–1443. https://doi.org/10.1016/j.marpetgeo.2011.05.008

Chakraborty, S. (2017). A new mechanism for upper crustal fluid flow driven by solitary porosity waves in rigid reactive media? *Geophysical Research Letters*, *44*(20), 10324–10327. https://doi.org/10.1002/2017gl075798

Connolly, J. A. D., & Podladchikov, Y. Y. (1998). Compaction-driven fluid flow in viscoelastic rock. *Geodinamica Acta*, *11*(2–3), 55–84. https://doi.org/10.1016/s0985-3111(98)80006-5

Connolly, J. A. D., & Podladchikov, Y. Y. (2007). Decompaction weakening and channeling instability in ductile porous media: Implications for asthenospheric melt segregation. *Journal of Geophysical Research*, *112*(B10). https://doi.org/10.1029/2005jb004213

Connolly, J. A. D., & Podladchikov, Y. Y. (2013). A hydromechanical model for lower crustal fluid flow. In *Metasomatism and the chemical transformation of rock* (pp. 599–658). Springer. https://doi.org/10.1007/978-3-642-28394-9_14

Connolly, J. A. D., Schmidt, M. W., Solferino, G., & Bagdassarov, N. (2009). Permeability of asthenospheric mantle and melt extraction rates at mid-ocean ridges. *Nature*, *462*(7270), 209–212. https://doi.org/10.1038/nature08517

Cruden, A. R. (1988). Deformation around a rising diapir modeled by creeping flow past a sphere. *Tectonics*, *7*(5), 1091–1101. https://doi.org/10.1029/tc007i005p01091

Dasgupta, R. (2018). Volatile-bearing partial melts beneath oceans and continents – Where, how much, and of what compositions? *American Journal of Science*, *318*(1), 141–165. https://doi.org/10.2475/01.2018.06

Davis, F., Hirschmann, M., & Humayun, M. (2011). The composition of the incipient partial melt of garnet peridotite at 3 GPa and the origin of OIB. *Earth and Planetary Science Letters*, *308*(3–4), 380–390. https://doi.org/10.1016/j.epsl.2011.06.008

Dohmen, J., & Schmeling, H. (2021). Magma ascent mechanisms in the transition regime from solitary porosity waves to diapirism. *Solid Earth*, *12*(7), 1549–1561. https://doi.org/10.5194/se-12-1549-2021

Dohmen, J., Schmeling, H., & Kruse, J. P. (2019). The effect of effective rock viscosity on 2-D magmatic porosity waves. *Solid Earth*, *10*(6), 2103–2113. https://doi.org/10.5194/se-10-2103-2019

Duretz, T., Räss, L., Podladchikov, Y., & Schmalholz, S. (2019). Resolving thermomechanical coupling in two and three dimensions: Spontaneous strain localization owing to shear heating. *Geophysical Journal International*, *216*(1), 365–379. https://doi.org/10.1093/gji/ggy434

Francis, D. (1976). The origin of amphibole in lherzolite xenoliths from Nunivak Island, Alaska. *Journal of Petrology*, *17*(3), 357–378. https://doi.org/10.1093/petrology/17.3.357

Gerya, T. (2019). *Introduction to numerical geodynamic modelling* (2nd ed.). Cambridge University Press. https://www.cambridge.org/core/books/abs/introduction-to-numerical-geodynamic-modelling/introduction/4FE9568364C73263E17D81CFD467AB81

Griffin, W., O'reilly, S. Y., Afonso, J. C., & Begg, G. (2009). The composition and evolution of lithospheric mantle: A re-evaluation and its tectonic implications. *Journal of Petrology*, *50*(7), 1185–1204. https://doi.org/10.1093/petrology/egn033

Harte, B., Hunter, R., & Kinny, P. (1993). Melt geometry, movement and crystallization, in relation to mantle dykes, veins and metasomatism. *Philosophical Transactions of the Royal Society of London, Series A: Physical and Engineering Sciences*, *342*(1663), 1–21. https://doi.org/10.1098/rsta.1993.0001

Herzberg, C. T. (1993). Lithosphere peridotites of the Kaapvaal craton. *Earth and Planetary Science Letters*, *120*(1–2), 13–29. https://doi.org/10.1016/0012-821x(93)90020-a

Herzberg, C. T., Baker, M. B., & Wendlandt, R. F. (1982). Olivine flotation and settling experiments on the join Mg_2SiO_4-Fe_2SiO_2. *Contributions to Mineralogy and Petrology*, *80*(4), 319–323. https://doi.org/10.1007/bf00378004

Hirano, N., Takahashi, E., Yamamoto, J., Abe, N., Ingle, S. P., Kaneoka, I., et al. (2006). Volcanism in response to plate flexure. *Science, New Series*, *313*(5792), 1426–1428. https://doi.org/10.1126/science.1128235

Hirose, K., & Kushiro, I. (1993). Partial melting of dry peridotites at high pressures: Determination of compositions of melts segregated from peridotite using aggregates of diamond. *Earth and Planetary Science Letters*, *114*(4), 477–489. https://doi.org/10.1016/0012-821x(93)90077-m

Hirschmann, M. M. (2010). Partial melt in the oceanic low velocity zone. *Physics of the Earth and Planetary Interiors*, *179*(1–2), 60–71. https://doi.org/10.1016/j.pepi.2009.12.003

Hirschmann, M. M., Kogiso, T., Baker, M. B., & Stolper, E. M. (2003). Alkalic magmas generated by partial melting of garnet pyroxenite. *Geology*, *31*(6), 481–484. https://doi.org/10.1130/0091-7613(2003)031<0481:amgbpm>2.0.co;2

Hofmann, A. (1972). Chromatographic theory of infiltration metasomatism and its application to feldspars. *American Journal of Science*, *272*(1), 69–90. https://doi.org/10.2475/ajs.272.1.69

Holland, T. J. B., & Powell, R. (1998). An internally consistent thermodynamic data set for phases of petrological interest. *Journal of Metamorphic Geology*, *16*(3), 309–343. https://doi.org/10.1111/j.1525-1314.1998.00140.x

Holtzman, B. K., & Kohlstedt, D. L. (2007). Stress-driven melt segregation and strain partitioning in partially molten rocks: Effects of stress and strain. *Journal of Petrology*, *48*(12), 2379–2406. https://doi.org/10.1093/petrology/egm065

Irving, A. J. (1980). Petrology and geochemistry of composite ultramafic xenoliths in alkali basalts and implications for magmatic processes within the mantle. *American Journal of Science*, *280*(A), 389–426.

Jackson, M. D., Blundy, J., & Sparks, R. S. J. (2018). Chemical differentiation, cold storage and remobilization of magma in the Earth's crust. *Nature*, *564*(7736), 405–409. https://doi.org/10.1038/s41586-018-0746-2

Jones, R. D. W., & Katz, R. F. (2018). Reaction-infiltration instability in a compacting porous medium. *Journal of Fluid Mechanics*, *852*, 5–36. https://doi.org/10.1017/jfm.2018.524

Jordan, J. S., & Hesse, M. A. (2015). Reactive transport in a partially molten system with binary solid solution. *Geochemistry, Geophysics, Geosystems*, *16*(12), 4153–4177. https://doi.org/10.1002/2015gc005956

Jordan, J. S., Hesse, M. A., & Rudge, J. F. (2018). On mass transport in porosity waves. *Earth and Planetary Science Letters*, *485*, 65–78. https://doi.org/10.1016/j.epsl.2017.12.024

Katz, R. F., Spiegelman, M., & Holtzman, B. (2006). The dynamics of melt and shear localization in partially molten aggregates. *Nature*, *442*(7103), 676–679. https://doi.org/10.1038/nature05039

Kelemen, P. B., Hirth, G., Shimizu, N., Spiegelman, M., & Dick, H. J. B. (1997). A review of melt migration processes in the adiabatically upwelling mantle beneath oceanic spreading ridges. *Philosophical Transactions of the Royal Society A: Mathematical, Physical & Engineering Sciences*, *355*, 283–318. https://doi.org/10.1098/rsta.1997.0010

Keller, T., May, D. A., & Kaus, B. J. P. (2013). Numerical modelling of magma dynamics coupled to tectonic deformation of lithosphere and crust. *Geophysical Journal International*, *195*(3), 1406–1442. https://doi.org/10.1093/gji/ggt306

Keller, T., & Suckale, J. (2019). A continuum model of multi-phase reactive transport in igneous systems. *Geophysical Journal International*, *219*(1), 185–222. https://doi.org/10.1093/gji/ggz287

Korzhinskii, D. (1965). The theory of systems with perfectly mobile components and processes of mineral formation. *American Journal of Science*, *263*(3), 193–205. https://doi.org/10.2475/ajs.263.3.193

Kushiro, I. (1996). Partial melting of fertile mantle peridotite at high pressures: An experimental study using aggregates of diamond. *Geophysical Monograph-American Geophysical Union*, *95*, 109–122. https://doi.org/10.1029/GM095p0109

Langmuir, C. H., Klein, E. M., & Plank, T. (1992). Petrological systematics of mid-ocean ridge basalts: Constraints on melt generation beneath ocean ridges. *Mantle flow and melt generation at mid-ocean ridges*, *71*, 183–280. https://doi.org/10.1029/GM071p0183

Llana-Fúnez, S., Wheeler, J., & Faulkner, D. R. (2012). Metamorphic reaction rate controlled by fluid pressure not confining pressure: Implications of dehydration experiments with gypsum. *Contributions to Mineralogy and Petrology*, *164*, 69–79. https://doi.org/10.1007/s00410-012-0726-8

Lloyd, F. E., & Bailey, D. K. (1975). Light element metasomatism of the continental mantle: The evidence and the consequences. *Physics and Chemistry of the Earth*, *9*, 389–416. https://doi.org/10.1016/b978-0-08-018017-5.50033-x

Malvoisin, B., Podladchikov, Y. Y., & Vrijmoed, J. C. (2015). Coupling changes in densities and porosity to fluid pressure variations in reactive porous fluid flow: Local thermodynamic equilibrium. *Geochemistry, Geophysics, Geosystems*, *16*(12), 4362–4387. https://doi.org/10.1002/2015gc006019

McKenzie, D. (1984). The generation and compaction of partially molten rock. *Journal of Petrology*, *25*(3), 713–765. https://doi.org/10.1093/petrology/25.3.713

McKenzie, D. (1985). The extraction of magma from the crust and mantle. *Earth and Planetary Science Letters*, *74*(1), 81–91. https://doi.org/10.1016/0012-821x(85)90168-2

McKenzie, D. (1989). Some remarks on the movement of small melt fractions in the mantle. *Earth and Planetary Science Letters*, *95*(1–2), 53–72. https://doi.org/10.1016/0012-821X(89)90167-2

Miller, R. B., & Paterson, S. R. (1999). In defense of magmatic diapirs. *Journal of Structural Geology*, *21*(8–9), 1161–1173. https://doi.org/10.1016/s0191-8141(99)00033-4

Müller, I. (2007). *A history of thermodynamics: The doctrine of energy and entropy*. Springer Science & Business Media. https://link.springer.com/book/10.1007/978-3-540-46227-9

Nauman, E. B., & He, D. Q. (2001). Nonlinear diffusion and phase separation. *Chemical Engineering Science*, *20*, 1999–2018. https://doi.org/10.1016/s0009-2509(01)00005-7

Nielson, J. E., & Noller, J. S. (1987). Processes of mantle metasomatism; constraints from observations of composite peridotite xenoliths. *Geological Society of America*, *215*, 61–76. https://doi.org/10.1130/spe215-p61

Nielson, J. E., & Wilshire, H. (1993). Magma transport and metasomatism in the mantle: A critical review of current geochemical models. *American Mineralogist*, *78*, 1117–1134. https://pubs.geoscienceworld.org/msa/ammin/article/78/11-12/1117/42713/Magma-transport-and-metasomatism-in-the-mantle-A

Omlin, S., Malvoisin, B., & Podladchikov, Y. Y. (2017). Pore fluid extraction by reactive solitary waves in 3-d. *Geophysical Research Letters*, *44*(18), 9267–9275. https://doi.org/10.1002/2017gl074293

Orr, F. M. (2007). *Theory of gas injection processes*. Tie-Line Publications. http://oildoc.ir/wp-content/uploads/2017/03/Theory-of-Gas-Injection-Processes-by-Franklin-M.-Orr-Jr.-%40Oildoc.pdf

Pilet, S., Abe, N., Rochat, L., Kaczmarek, M. A., Hirano, N., & Machida, S. (2016). Pre-subduction metasomatic enrichment of the oceanic lithosphere induced by plate flexure. *Nature Geoscience*, *9*(12), 898–903. https://doi.org/10.1038/ngeo2825

Pilet, S., Baker, M. B., & Stolper, E. M. (2008). Metasomatized lithosphere and the origin of alkaline lavas. *Science*, *320*(5878), 916–919. https://doi.org/10.1126/science.1156563

Plümper, O., John, T., Podladchikov, Y. Y., Vrijmoed, J. C., & Scambelluri, M. (2016). Fluid escape from subduction zones controlled by channel-forming reactive porosity. *Nature Geoscience*, *10*(2), 150–156. https://doi.org/10.1038/ngeo2865

Räss, L., Duretz, T., & Podladchikov, Y. Y. (2019). Resolving hydromechanical coupling in two and three dimensions: Spontaneous channelling of porous fluids owing to decompaction weakening. *Geophysical Journal International*, *218*(3), 1591–1616. https://doi.org/10.1093/gji/ggz239

Schmalholz, S. M., Moulas, E., Plümper, O., Myasnikov, A. V., & Podladchikov, Y. Y. (2020). 2D hydro-mechanical-chemical modeling of (de)hydration reactions in deforming heterogeneous rock: The Periclase-Brucite model reaction. *Geochemistry, Geophysics, Geosystems*, *21*(11). https://doi.org/10.1029/2020gc009351

Schmeling, H., Marquart, G., Weinberg, R., & Wallner, H. (2019). Modelling melting and melt segregation by two-phase flow: New insights into the dynamics of magmatic systems in the continental crust. *Geophysical Journal International*, *217*(1), 422–450. https://doi.org/10.1093/gji/ggz029

Scott, D. R., & Stevenson, D. J. (1984). Magma solitons. *Geophysical Research Letters*, *11*(11), 1161–1164. https://doi.org/10.1029/gl011i011p01161

Scott, D. R., Stevenson, D. J., & Whitehead, J. A. (1986). Observations of solitary waves in a viscously deformable pipe. *Nature*, *319*(6056), 759–761. https://doi.org/10.1038/319759a0

Shaw, H. R. (1980). The fracture mechanisms of magma transport from the mantle to the surface. In *Physics of magmatic processes* (pp. 201–264). Princeton University Press. https://doi.org/10.1515/9781400854493.201

Spiegelman, M. (1993). Physics of melt extraction: Theory, implications and applications. *Philosophical Transactions of the Royal Society of London, Series A: Physical and Engineering Sciences*, *342*(1663), 23–41. https://doi.org/10.1098/rsta.1993.0002

Spiegelman, M., Kelemen, P. B., & Aharonov, E. (2001). Causes and consequences of flow organization during melt transport: The reaction infiltration instability in compactible media. *Journal of Geophysical Research*, *106*(B2), 2061–2077. https://doi.org/10.1029/2000jb900240

Stevenson, D. J. (1989). Spontaneous small-scale melt segregation in partial melts undergoing deformation. *Geophysical Research Letters*, *16*(9), 1067–1070. https://doi.org/10.1029/gl016i009p01067

Tomlinson, E. L., & Kamber, B. S. (2021). Depth-dependent peridotite-melt interaction and the origin of variable silica in the cratonic mantle. *Nature Communications*, *12*(1), 1082. https://doi.org/10.1038/s41467-021-21343-9

Walker, D., Stolper, E. M., & Hays, J. F. (1978). A numerical treatment of melt/solid segregation: Size of the eucrite parent body and stability of the terrestrial low-velocity zone. *Journal of Geophysical Research*, *83*(B12), 6005–6013. https://doi.org/10.1029/jb083ib12p06005

Wallace, M., & Green, D. (1988). An experimental determination of primary carbonatite magma composition. *Nature*, *335*, 343–346. https://doi.org/10.1038/335343a0

Walter, M. J. (1998). Melting of garnet peridotite and the origin of komatiite and depleted lithosphere. *Journal of Petrology*, *39*(1), 29–60. https://doi.org/10.1093/petroj/39.1.29

Wass, S. Y., & Roge, N. W. (1980). Mantle metasomatism-precursor to continental alkaline volcanism. *Geochimica et Cosmochimica Acta*, *44*(11), 1811–1823. https://doi.org/10.1016/0016-7037(80)90230-6

Wasylenki, L. E., Baker, M. B., Kent, A. J. R., & Stolper, E. M. (2003). Near-solidus melting of the shallow upper mantle: Partial melting experiments on depleted peridotite. *Journal of Petrology*, *44*(7), 1163–1191. https://doi.org/10.1093/petrology/44.7.1163

Weatherley, S. M., & Katz, R. F. (2012). Melting and channelized magmatic flow in chemically heterogeneous, upwelling mantle. *Geochemistry, Geophysics, Geosystems*, *13*(5). https://doi.org/10.1029/2011gc003989

Weinberg, R. F., & Podladchikov, Y. (1994). Diapiric ascent of magmas through power law crust and mantle. *Journal of Geophysical Research*, *99*(B5), 9543–9559. https://doi.org/10.1029/93jb03461

Wilshire, H. (1987). A model of mantle metasomatism. *Mantle Metasomatism and Alkaline Magmatism. Geological Society of America, Special Papers*, *215*, 47–60. https://doi.org/10.1130/spe215-p47

Yarushina, V. M., & Podladchikov, Y. Y. (2015). (De)compaction of porous viscoelastoplastic media: Model formulation. *Journal of Geophysical Research: Solid Earth*, *120*(6), 4146–4170. https://doi.org/10.1002/2014jb011258

Yarushina, V. M., Wang, L. H., Connolly, D., Kocsis, G., Fæstø, I., Polteau, S., & Lakhlifi, A. (2021). Focused fluid-flow structures potentially caused by solitary porosity waves. *Geology*. https://doi.org/10.1130/g49295.1